Chapter 3

Doxorubicin Intercalated Li-Al Based LDHs as Potential Drug Delivery Nano-vehicle with pH-responsive Therapeutic Cargo for Tumor Treatment

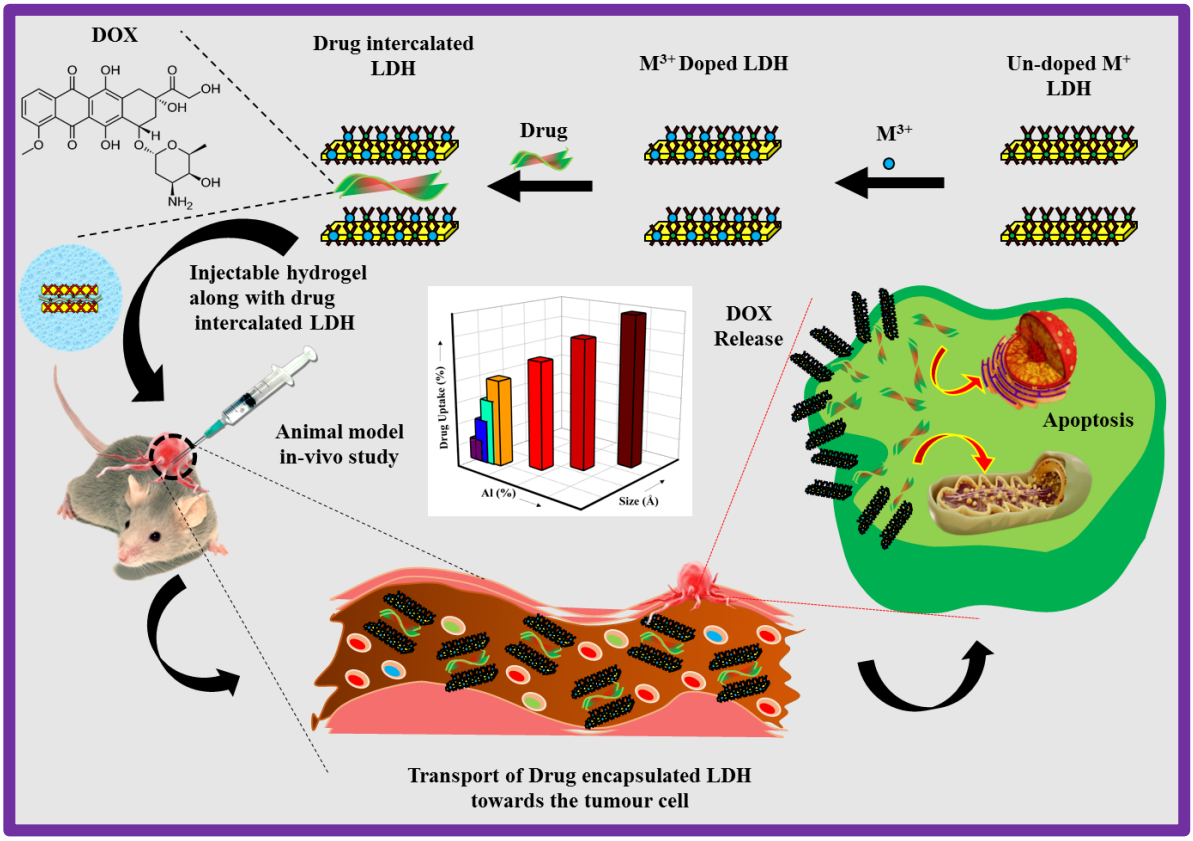

3.1 Introduction

In recent decades, awareness of cancer as a lethal disease with a high global mortality rate has increased. Research efforts continue to address this daunting illness. While surgery, chemotherapy, and radiotherapy are established treatments, each approach has notable drawbacks [1, 2]. Chemotherapy, a widely used cancer treatment, aims to kill cancer cells or slow their growth; however, it often results in severe side effects, such as damage to healthy cells and immune system compromise, leading to adverse effects like nausea, appetite loss, myelosuppression, mucositis, and alopecia [3]. Key challenges include effective cellular internalization and target-specific delivery of anticancer drugs. Traditional direct delivery methods face issues such as enzymatic degradation, low bioavailability, poor circulatory stability, and negative effects from carrier accumulation. Therefore, there is an ongoing need for effective and safe drug delivery systems [4]. Enhancements to existing anticancer medications and drug delivery vectors, both viral and nonviral, have been pursued to boost their potential and efficiency for cellular uptake in malignant tumor cells [5]. Targeted delivery is particularly sought after in cancer therapy to improve therapeutic and diagnostic outcomes while minimizing adverse effects. New sustained drug-release vehicles are being designed to overcome limitations of traditional methods by releasing drugs in a controlled manner in response to stimuli or over time, thereby extending drug presence in the bloodstream [6-8]. The integration of modern biology, medicine, and nanotechnology has opened up significant clinical opportunities for tumor therapy, revolutionizing traditional cancer management approaches [9-11]. Inorganic-based nanoplatforms are emerging as promising nano-biomaterials due to their versatile functionality, enhanced quality control, and cost-effectiveness [12-14]. Thus, the development of novel inorganic nanomaterials that maintain pharmacological advantages while meeting safety requirements remains crucial.

Recently, various 2D nanomaterials have garnered significant attention in medicine due to their quantum size and surface effects [15-17]. Nanomaterials such as graphene [18], transition-metal dichalcogenides [19], hexagonal boron nitride [20], amorphous calcium carbonate [21], and black phosphorus [22] have been studied as carriers for drug loading and have shown promise in cancer treatment. However, many 2D nanomaterials depend on a "top-down" mechanical exfoliation method, which poses challenges in controlling thickness, particle size, shape, and homogeneity [23-24]. Additionally, 2D nanomaterials often exhibit low drug loading capacity (DLC) and encapsulation efficiency (EE), which can be affected by the interactions between the nanocarrier and the drug. Consequently, developing new drug formulations based on 2D nanomaterial designs, while ensuring structured regulation and effective cancer therapy, remains a significant challenge. To stabilize therapeutic biofunctionalized compounds, such as oligonucleotides and anticancer drugs, LDHs have been created as inorganic nanoparticles [25-31]. These LDHs can stabilize various anionic biofunctionalized molecules between their positively charged brucite-like layers through electrostatic interactions [32, 33]. LDH nanocarriers are effective for gene and chemotherapy delivery due to their low cellular toxicity and clathrin-mediated endocytosis. Anionic drugs can be incorporated into LDH layers via ion exchange, as represented by the general formula of LDH : , $[M^{II}_{1-x}M^{III}_{x}\ (OH)_2]^{x+}\ [(A^{m-})_{x/m}\ .\ n(H_2O)]^{x-}$,where M^{II} and M^{III} represent divalent and trivalent metal ions, respectively, and Am- denotes the interlayer anion [4]. While the combination of M^{II} and M^{III} is well-documented, the Li-Al based LDHs represent the only known example of M^{I}-M^{III} LDHs [34]. Research has analyzed LDHs in terms of free energy [35], structure [36], and anion intercalation [37], and hydration states [38] by modifying intra-layer metal ions.

Fogg et al. utilized molecular dynamics simulations to elucidate the structure of LiAl-X compounds (X = Br^-, Cl^-, NO_3^-, CO_3^{2-}, SO_4^{2-}, $C_2O_4^{2-}$), examining interlayer spacing and

ion orientations [39]. Density functional theory (DFT) was employed to explore the structural stability of LiAl-X compounds [40]. Additionally, molecular dynamics simulations tracked positional changes of Cl− ions in LiAl-Cl over a temperature range of -90 to 90°C [41]. Among various Li-Al based LDHs, LiAl-Cl-mH2O is the only compound known to undergo delithiation [42]. These materials are attractive due to their superior anion exchange capacity, biocompatibility, low toxicity, and ability to form well-structured suspensions suitable for injectable formulations. The protonation of OH groups around metal ions on positively charged LDHs enables the delivery of intracellular drugs in response to the acidic tumor microenvironment, facilitating incorporation into cancer cells. Anionic drugs, such as methotrexate and 5-fluorouracil, have been effectively delivered using LDHs, demonstrating their potential as drug carriers [43].

It is important to note that enhancing tumor treatment hinges not only on developing biocompatible nanomaterials but also on identifying and utilizing effective therapeutic pathways. Currently, apoptosis-based mechanisms are key targets in modern cancer treatments. For instance, doxorubicin (DOX), a commonly used antitumor antibiotic, induces apoptosis in tumor cells through two primary mechanisms: (i) intercalating into cancer cell DNA and inhibiting topoisomerase II-mediated DNA replication, and (ii) inducing mitochondrial apoptosis by generating semiquinone radicals [44]. DOX also shows promise for developing new anticancer drugs by leveraging these cytotoxic pathways, demonstrating clinically relevant efficacy against various tumor types.

In this study, Li-Al based LDHs were synthesized using coprecipitation methods while varying elemental compositions. DOX was incorporated through ion exchange, and DFT was utilized to analyze the interactions and structure of DOX-intercalated LDHs. Sustained drug delivery was achieved with different dimensional LDHs. Antitumor efficacy and toxicity were assessed through *in vitro* and *in vivo* drug release profiles, comparing DOX

intercalated LDHs with pristine DOX. The link between the anti-proliferative effect and apoptotic signalling was investigated through protein expression analysis via western blotting. The novel nanoformulation was tested *in vivo* on melanoma-bearing mice to evaluate tumor growth suppression and ensure no significant adverse effects on vital organs.

3.2 Results and Discussion

3.2.1 Evaluation of chemical formula and basic characterizations of the nanocarriers and drug loaded nanocarriers

The tumor-targeting Li-Al based LDH nanocarriers, along with doxorubicin (DOX) intercalated Li-Al LDHs, were synthesized using a coprecipitation method. Variants of LDH nanocarriers (LDH1, LDH2, and LDH3) were produced by altering the ratios of lithium and aluminium. The chemical formulas of LDH1, LDH2, and LDH3 nanocarriers were elucidated through XPS studies, **Table 3.1**, leading to the conclusion of a general chemical formula for layered double hydroxides (LDH) with a combination of M^{+} and M^{3+} ions.

General formula of M^{1+} / M^{3+} type LDHs

$$[M^{+}_{1-x}\, M^{3+}_{x}\, (OH)]^{2x+}\, [(A^{m-})_{2x/m} \cdot n(H_2O)]^{2x-}$$

Samples Name	Chemical Formula	Cation substitution ratio, $x = [M^{3+}]/[M^{1+} + M^{3+}]$
LDH 1	$[Li^{+}_{0.36}\, Al^{3+}_{0.64}\, (OH)]^{(2\times0.64)+}\, [(NO_3^{-})_{2\times0.64/1} \cdot n(H_2O)]^{(2\times0.64)-}$	0.64
LDH 2	$[Li^{+}_{0.33}\, Al^{3+}_{0.67}\, (OH)]^{(2\times0.67)+}\, [(NO_3^{-})_{2\times0.67/1} \cdot n(H_2O)]^{(2\times0.67)-}$	0.67
LDH 3	$[Li^{+}_{0.25}\, Al^{3+}_{0.75}\, (OH)]^{(2\times0.75)+}\, [(NO_3^{-})_{2\times0.75/1} \cdot n(H_2O)]^{(2\times0.75)-}$	0.75

Table 3.1 Proposed general formula of M^{1+}/ M^{3+} type LDHs which can be justified by theoretically, where x is the cation substitution ratio (evaluated from XPS analysis), m is the number of anionic charge and n is the number of entrapped water molecule. In this work, by varying the Li and Al elements, we mainly synthesize three nanocarriers (detailed discussed in synthesize section) named LDH1, LDH2 and LDH3. From LDH1 to LDH3, we gradually increase in aluminium concentration which can be justified by all elemental characterizations such as HRSEM and XPS analysis. The value of cation substitutions ratio (x) of LDH1, LDH2 and LDH3 are 0.64, 0.67 and 0.75 respectively. Here we mention the chemical formula of LDH1, LDH2 and LDH3 by using XPS analysis along with maintaining the charge balance.

XPS analysis revealed a notable increase in the binding energy of Al 2p, shifting from LDH1 to LDH3, with values rising from 74 to 74.3 eV. A similar trend was observed for Li 1s, with binding energy increasing from 54.8 to 55.2 eV for LDH1 to LDH3, in **Figure**

3.1.a). This corresponds to an increase in the cation substitution ratio (x) from 0.64 to 0.75. The general chemical formula for M^{+}/M^{3+} type LDHs, $[M^{+}_{1-x}\ M^{3+}_{x}\ (OH)]^{2x+}[(A^{m-})_{2x/m}\ .\ n(H_2O)]^{2x-}$, was established based on the cation substitution values in the information (**Table 3.1**). The progressive increase in binding energy for Al 2p, Li 1s, and cation substitution ratio from LDH1 to LDH3 indicates enhanced atomic mobility, potentially leading to structural distortions within the crystal lattice. Additionally, XPS revealed an increase in the atomic percentage ratio of Al/Li and the area under the curve for (Al 2p)/(Li 1s), with values changing from 1.82 to 3 and 19.9 to 23, respectively .

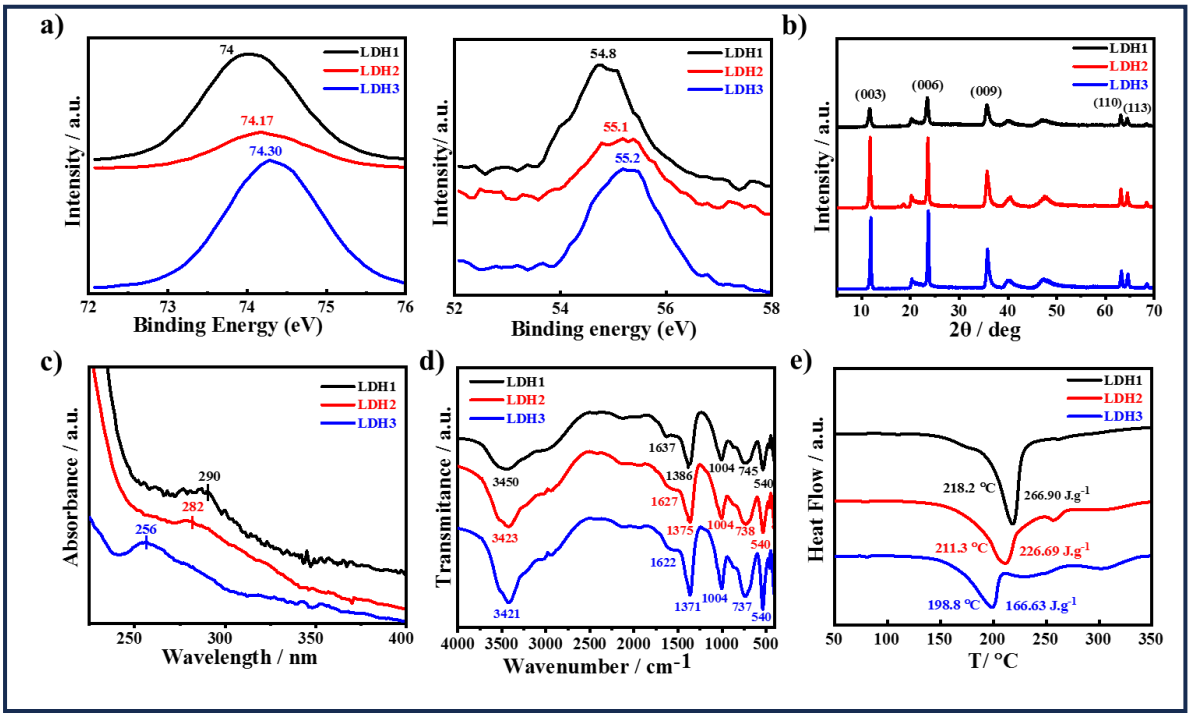

Figure 3.1: Characterizations along with understanding the nature of Li-Al based LDHs nanocarriers. **a)** Comparative XPS spectra for Al 2p (left) and Li 1s (right) in LDH1, LDH2 and LDH3 nanocarriers, interestingly the binding energy value for both Al 2p and Li 1s cases slightly increases from LDH1 to LDH3; **b)** Powder X-ray diffraction patterns of LDH1, LDH2 and LDH3 nanocarriers; **c)** Comparative representation of solid state UV-Vis spectra of different indicated nanocarriers; **d)** FTIR spectra of the nanocarriers,

displaying a shift in peak position from LDH1 to LDH3 nanocarriers by increasing the percentage of aluminium; and **e)** DSC thermograms of the indicated nanocarriers mentioning the melting temperature and heat of fusion.

The structural properties of the LDH nanocarriers were characterized through powder XRD, which displayed distinct peaks corresponding to the (003), (006), and (009) crystalline planes, alongside well-defined (110) and (113) peaks (**Figure.3.1.b**). The typical (003) reflection revealed a variation in basal spacing and crystalline domain size, which decreased from 0.76 to 0.74 nm and increased from 32.2 to 69.3 nm, respectively, across LDH1 to LDH3. Drug-loaded LDHs showed a basal spacing of 0.74 nm , with crystalline domain sizes increasing from 38 to 46.2 nm for DOX@LDH1 to DOX@LDH3 (**Figure 3.2.a,b**). The compositional differences in Li-Al based LDH nanocarriers and their drug intercalation capabilities were assessed using solid-state diffuse reflection UV/Vis spectroscopy. The pristine LDH1, LDH2, and LDH3 nanocarriers exhibited UV absorption peaks at 290, 282, and 256 nm, respectively, (**Figure 3.1.c**) attributed to the presence of intercalated nitrate anions. Pure DOX displayed a peak at 268 nm [45]. The peaks shifted to 303 nm ($\Delta\lambda$ = 13 nm) for DOX@LDH1 and 292 nm ($\Delta\lambda$ = 36 nm) for DOX@LDH3), indicating a significant red shift that suggests strong interactions with DOX (**Figure 3.2.c**). The more pronounced redshift in DOX@LDH3, which contains a higher aluminium content, indicates that this nanocarrier forms a more stable nanoformulation compared to DOX@LDH1. The compositional changes following aluminium content variation were further corroborated by Fourier Transform Infrared Spectroscopy (FTIR). The O–H stretching vibrations of LDH1 to LDH3 decreased from 3450 to 3421 cm^{-1}, while the bending vibrations of interlayer water molecules diminished from 1637 to 1622 cm^{-1}. The ν-3 stretching vibration of the NO_3^- groups also showed a systematic decline from 1386 to

1371 cm^{-1}. Additionally, there were minor decreases in the M–O vibrations for LDH1 to LDH3, with a peak at 540 cm^{-1} indicative of M–O–H bending for all three nanocarriers (**Figure 3.1.d**). The aforementioned peaks shifted to lower wavenumbers for the drug-loaded nanocarriers [43], confirming effective interactions between the drug and the pristine LDH nanocarriers .The additional peaks at 1586 and 1583 cm^{-1} for DOX@LDH1 and DOX@LDH3, respectively (**Figure 3.2.d**), correspond to the C=C stretching of the aromatic ring, affirming the incorporation of doxorubicin into the system [46].

DSC was conducted to evaluate the capacity of the synthesized nanocarriers to protect the encapsulated drug molecules from thermal degradation and to assess the interaction between the drug and various Li-Al based LDH nanocarriers as host materials. The melting temperatures and heats of fusion exhibited a decreasing trend from LDH1 to LDH3, with melting points of 218°, 211°, and 199 °C, and heats of fusion decreasing from 266.9 to 166.6 J/g indicating (**Figure 3.1.e**) gradual decreasing trend of melting temperature and heat of fusion with increasing the percentage of Al which further justify somewhat distorted crystal structure of LDHs at higher percentage of Al. The melting point of DOX loaded LDHs (both DOX@LDH1 and DOX@LDH3 nanoformulation) exhibit melting at 168°C, lowered from the melting point of pristine DOX at 217 °C along with considerable reduction of heat of fusion (**Figure 3.2.e**).

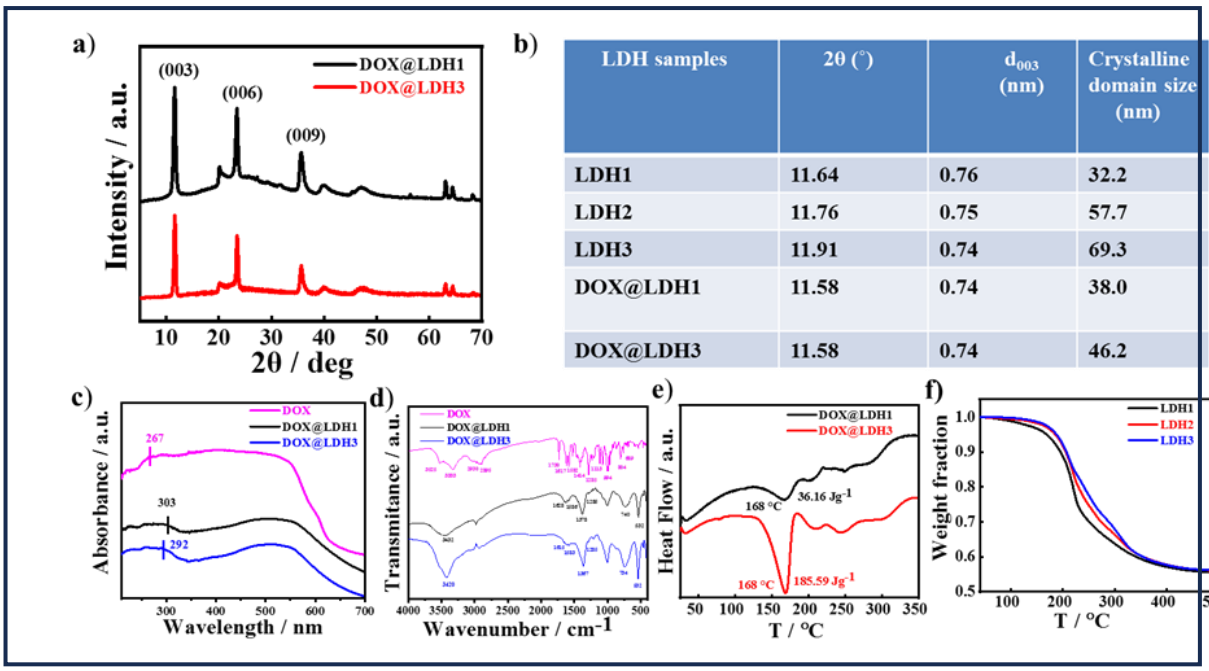

LDH samples	2θ (°)	d_{003} (nm)	Crystalline domain size (nm)
LDH1	11.64	0.76	32.2
LDH2	11.76	0.75	57.7
LDH3	11.91	0.74	69.3
DOX@LDH1	11.58	0.74	38.0
DOX@LDH3	11.58	0.74	46.2

Figure 3.2: a) Powder (XRD) of DOX intercalated Li-Al based LDHs nanoformulations named DOX@LDH1 and DOX@LDH3; **b)** XRD data table which reflects the slightly decreasing trend of d_{003} spacing of (003) plane from LDH1 to LDH3 but crystalline domain size (calculated from Debye-Scherrer equation) gradually increases from LDH1 to LDH3. In the case for DOX intercalated systems i.e. DOX@LDH1 and DOX@LDH3, d_{003} spacing are equal in both of the cases but crystalline domain size increases from DOX@LDH1 to DOX@LDH3, this is mainly due to the large sized nanocarrier LDH3; **c)** Solid state UV-Vis spectra of DOX, DOX@LDH1 and DOX@LDH3. In case of DOX, the peak arises in 267 nm but when it is incorporated into the nanocarriers LDH1 and LDH3 formed nanoformulation DOX@LDH1 and DOX@LDH3, the peak is shifted to higher wavelength region such as 303 and 292 nm indicating strong interaction between drug molecule and nanocarriers; **d)** FTIR spectra of pristine DOX along with nanoformulations DOX@LDH1 and DOX@LDH3 showing shifting in peak positions due to interactions. The major peak position of drug molecule (DOX) arises in 3333, 1617, 1582 cm^{-1} which is shifted 3432, 1628, 1586 cm^{-1} and 3420, 1615, 1583 cm^{-1} for DOX@LDH1 and DOX@LDH3, respectively; **e)** DSC thermograms of DOX@LDH1 and DOX@LDH3 indicating the

melting temperature and heat of fusion values. The melting temperature of pristine DOX is 217°C which is shifted to 168°C in both of the cases. Interestingly, the heat of fusion of DOX@LDH3 is quite high (185.59 $J.g^{-1}$) as compared to the DOX@LDH1 (36.16 $J.g^{-1}$); **f)** TGA thermograms of LDH1, LDH2 and LDH3 nanocarriers with their relative thermal stability**.** 5 % degradation temperature of LDH1, LDH2 and LDH3 are 168, 185 and 188°C respectively showing higher thermal stability of LDH3 compared to others.

This indicates a robust interaction between the LDH nanocarriers and the drug molecules. These results demonstrate that nanocarriers with a higher aluminium content exhibit enhanced thermal stability. Thus, both DSC and TGA analyses confirm the thermal stability of the nanocarriers and their strong interactions with DOX, suggesting that these formulations effectively protect DOX from thermal degradation, positioning them as promising candidates for anti-cancer applications.

3.2.2 Shape, size and properties of the nanocarriers

LDHs have been synthesized using lithium (Li) and aluminium (Al) salts, allowing for variations in their composition, specifically Li and Al, while maintaining consistent scientific rigor regarding size, shape, zeta potential, and surface area. This enables the development of effective carriers for bioactive molecule delivery (such as drugs and genes). Three distinct Li-Al based LDH nanocarriers - LDH1, LDH2, and LDH3 - were created by altering the ratios of Li and Al, and their size, shape, zeta potential, surface area, and morphology were thoroughly examined. The hexagonal morphology of the particles showed an increase in size from LDH1 to LDH3, specifically measuring 65±5 nm, 109±3 nm, and 146±4 nm, respectively, as determined by high-resolution scanning electron microscopy (HRSEM, **Figure 3.3.a**). Bright field TEM images confirmed a similar

hexagonal plate-like structure with lateral dimensions increasing from 50±6 nm for LDH1 to 185±6 nm for LDH3 (**Figure 3.3.b**) . DLS results corroborated the size trends observed in HRSEM and HRTEM, illustrating a consistent increase in particle size associated with higher Al content. The zeta potential measurements displayed a systematic decline from 28 mV for LDH1 to 12 mV for LDH3 (**Figure 3.3.c**).

The nanocarriers exhibit a positive and elevated zeta potential, making them suitable for use as delivery vehicles into negatively charged cells. Notably, smaller particles tend to have a higher absolute zeta potential than larger ones, likely due to their increased reactivity and impact [47]. AFM analysis confirms that all nanocarriers possess particle characteristics, with those containing higher aluminium content displaying larger sizes (**Figure 3.3.d**) . The surface area of the nanocarriers was assessed using Brunauer-Emmett-Teller (BET) studies, revealing that the smaller particles (LDH1) have a higher surface area of 39 m^2/g compared to just 11 m^2/g for LDH3. These findings indicate a gradual increase in particle size from LDH1 to LDH3 (**Figure 3.3.e**), reflecting a proportional relationship between size and the increasing aluminium content, attributed to the greater coordination number of aluminium in comparison to lithium [48].

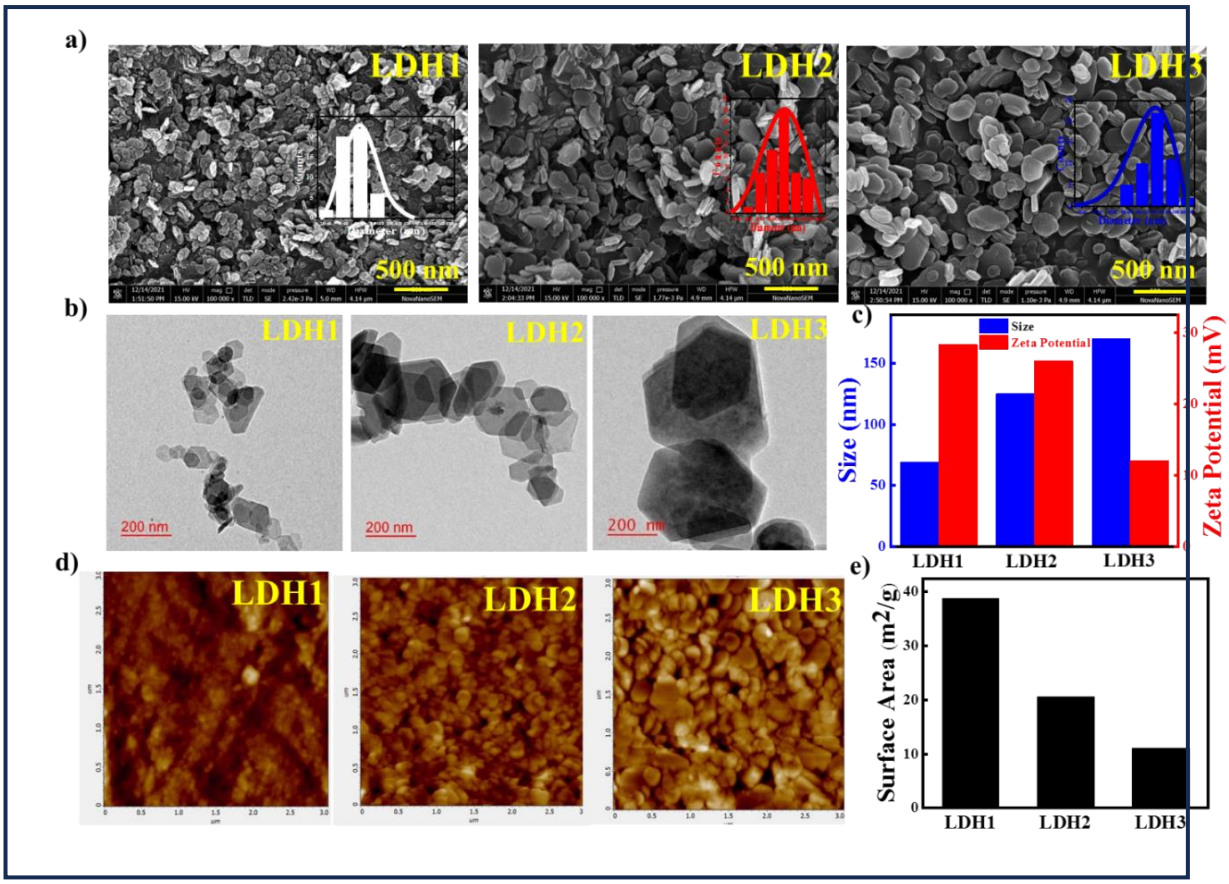

Figure 3.3: Size and morphological analysis of different Li-Al based LDHs nanocarriers along with their relevant properties, **a)** HRSEM images of LDH1, LDH2 and LDH3 nanocarriers: Size gradually increases from LDH1 to LDH3 with hexagonal morphology. The histogram analysis of the nanocarriers size distribution are shown in the individual inset; **b)** HRTEM microscopic image of hexagonal like morphology with increasing trend of size from LDH1 to LDH3 confirming the results obtained from HRSEM. From LDH1 to LDH3, increasing percentage of aluminium (Al) results towards increasing trend of size; **c)** the hydrodynamic diameter and zeta potential of LDH1, LDH2 and LDH3 nanocarriers were determined using dynamic light scattering (DLS), and justify the results obtained from HRSEM and HRTEM *i.e.* increasing trend of size from LDH1 to LDH3; **d)** AFM images of LDH1, LDH2 and LDH3 (3×3 μm^2) measured through semi-contact mode; and **e)**

Evaluation of surface area for LDH1, LDH2 and LDH3 nanocarriers indicating large surface area for smaller size particle.

3.2.3 Encapsulation and Sustained Release Profile of DOX in Li-Al Based LDHs along with Theoretical Understanding of Interaction

The incorporation of nitrate ions as intercalant in LDHs facilitates the encapsulation of negatively charged drugs like DOX through an ion exchange mechanism. The encapsulation process was conducted with an excess of drug in solution, resulting in a drug loading capacity (DLC) of 51% for DOX@LDH1 and 60% for DOX@LDH3 formulations. The increased drug loading capacity in DOX@LDH3 can be attributed to its larger particle size, which is a consequence of a higher aluminium content leading to a greater coordination number. This variation in dimension among LDHs allows for regulated drug encapsulation, with DOX@LDH3 exhibiting superior encapsulation efficiency, primarily due to extensive hydrogen bonding between the LDH and DOX, as indicated by a notable shift in the FTIR peak (from 1622 cm^{-1} to 1583 cm^{-1}) and a significant red shift in UV absorption (from 256 nm to 292 nm). Thus, DOX@LDH3 proves to be a more effective vehicle for drug delivery.

The efficacy of the anticancer drug DOX relies heavily on its sustained release, which is influenced by the vehicle design and the effective release from Li-Al based LDHs nanocarriers. Consequently, the release profiles of DOX from DOX@LDH1 and DOX@LDH3 were evaluated in buffer solutions mimicking a biological environment, with variations in pH. The UV absorbance of the supernatant was recorded at 480 nm to monitor the release. After 12 hours of incubation in phosphate-buffered saline (PBS) at pH ~7.4, the percentage release of DOX was found to be 15% for DOX@LDH1 and 9% for DOX@LDH3 (**Figure. 3.4.a**). Both formulations displayed a slower, sustained release,

with DOX@LDH3 demonstrating a more favourable release profile. This enhanced stability in physiological conditions is primarily due to better encapsulation of DOX facilitated by stronger hydrogen bonding in the larger LDH3 structure compared to the smaller LDH1.Furthermore, pH-dependent drug release studies were conducted to simulate tumor microenvironments, revealing significantly higher release percentages of 35% and 68% at pH 6 and 4, respectively, after 12 hours (**Figure.3.4.b**). The markedly increased drug release at lower pH levels indicates effective targeted delivery to tumor tissues, which are characterized by acidic conditions, in contrast to minimal drug release at normal tissue pH (>6). Importantly, DOX@LDH3 shows a capacity for preferentially delivering the drug to tumor tissues, evidenced by the comparative release rates of 68% and 9% in acidic versus normal pH conditions, reflecting the vehicle's responsiveness to the endosomal/lysosomal environment. Sustained release is vital for cancer treatment, as it helps maintain drug concentrations within a therapeutic range for extended periods, thereby minimizing side effects. While many organic and inorganic nanoparticles are susceptible to hydrolysis even in neutral pH, our results indicate that the designed Li-Al based LDHs nanocarrier exhibits significantly improved resistance to acidic conditions, making it suitable for drug delivery applications.

To elucidate the drug release mechanism, several factors contribute, including drug diffusion from the nanocarrier matrix and solvent penetration into the matrix, both of which influence release kinetics. Various kinetic models, such as zero-order, first-order, Higuchi, and Korsmeyer-Peppas, were applied to assess the release profiles in **Figure.3.5 (a, b, c, d**) from DOX@LDH1 and DOX@LDH3. The linear correlation coefficients (r^2) indicate a better fit for the Higuchi and Korsmeyer-Peppas models, with values of 0.96 and 0.99 for DOX@LDH1 and DOX@LDH3, respectively. The release exponent (n), which indicates the transport mechanism, was calculated to be 0.45 for DOX@LDH1 and 0.4 for

DOX@LDH3, suggesting a quasi-Fickian diffusion mechanism with non-swellable matrix diffusion [49]. The molecular assembly responsible for regulated drug release in relation to particle size differences is illustrated in **Figure. 3.4.c**, highlighting the stronger hydrogen bonding interactions and larger confinement in DOX@LDH3 compared to DOX@LDH1. This suggests a better-controlled drug release mechanism, crucial for maintaining therapeutic drug levels in circulation over prolonged periods, essential for effective cancer treatment.

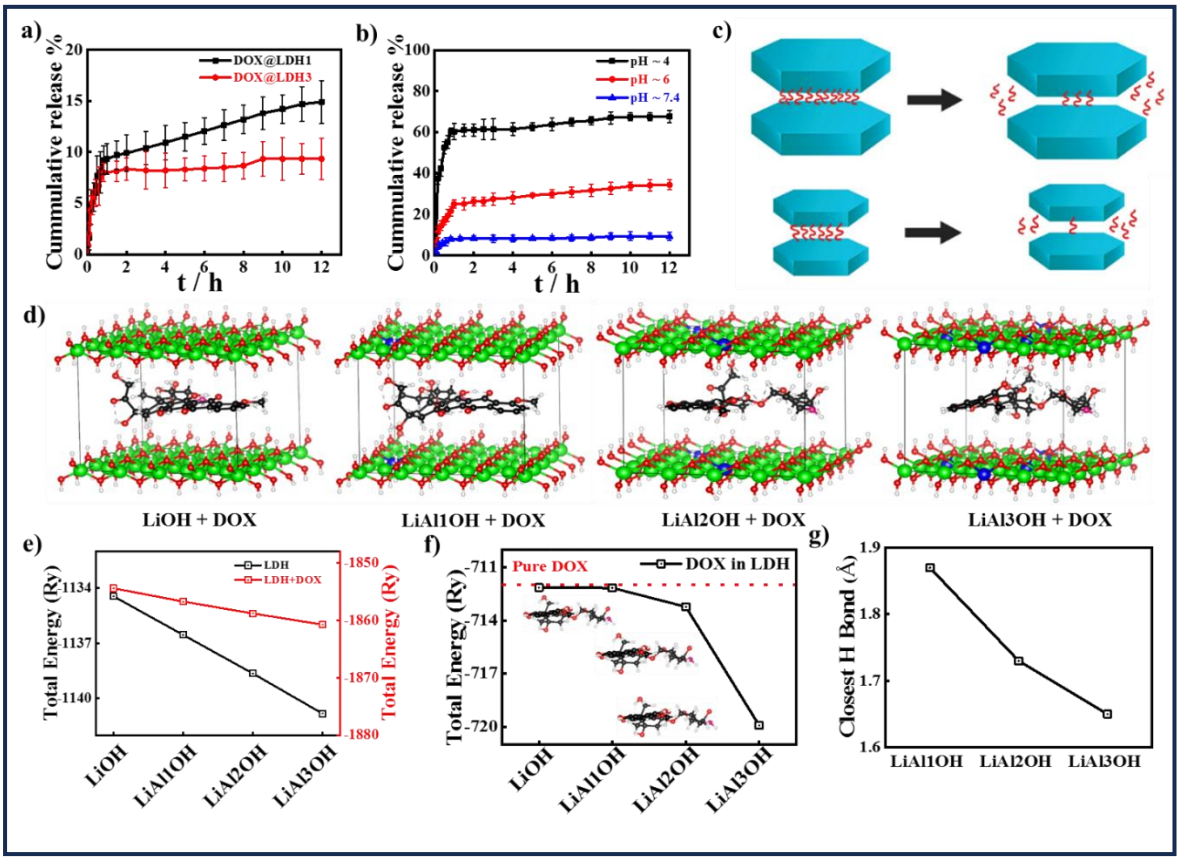

Figure 3.4: Size dependency along with pH-triggered drug release features from the designed nanoformulation and strong interaction between DOX and Li-Al based LDHs. **a)** Comparative cumulative drug release profile of DOX loaded LDHs (DOX@LDH1 and DOX@LDH3) in PBS at a particular pH ~7.4 at 37 °C; **b)** Comparative release profiles of DOX from DOX@LDH3 in PBS in various pH media (pH ~7.4, 6 and 4 at 37 °C. Data expressed as mean value ±SD (n=3); **c)** Schematic diagram illustrating the release of drugs

from different size nanovehicles. Large size nanovehicle (DOX@LDH3) exhibit sustained drug release because of greater confinement and stronger interaction whereas small size nanocarrier (DOX@LDH1) shows a burst release of drug; **d)** Theoretical evaluation of interaction between DOX molecule and different Li-Al based LDHs nanoformulation with increase in doping aluminium (Al) concentration into the lithium hydroxide (LiOH) crystal for representative systems of LiOH+DOX, LiAl1OH+DOX, LiAl2OH+DOX and LiAl3OH+DOX nanoformulations having representing color codes of different atoms: blue-Aluminium, green-Lithium, red-Oxygen, white- Hydrogen, pink-Nitrogen, and black-Carbon; **e)** Variation of total energy of Li-Al based LDHs and DOX loaded LDHs (LDH+DOX) nanoformulations before and after interaction between DOX and different nanocarriers (LiOH, LiAl1OH, LiAl2OH and LiAl3OH); **f)** Comparative study of total energy of free DOX molecule and DOX molecule intercalated in different Li-Al based LDHs nanocarriers; and **g)** Comparative analyses of closest H-bonded distance between DOX molecule and H- atom in Li-Al based LDHs nanocarriers in different indicated nano formulations.

To comprehend the interactions that govern release behavior, the crystal structure of Li-Al based LDHs ($Li_{1-x}Al_xOH$) was modelled by doping aluminium (Al) atoms into the lithium hydroxide (LiOH) crystal structure at various concentrations. The LiOH structure is tetragonal, belonging to the P4/nmm space group, with lattice parameters a = 4.93 Å, b = 4.94 Å, and c = 4.28 Å. Structures of LiOH were sourced from the Materials Project database [50] featuring one LiOH sheet oriented in the (0, 0, 1) direction. In this structure, Li^+ ions are coordinated to four equivalent O^{2-} atoms, forming distorted corner and edge-sharing LiO4 tetrahedra, with all Li–O bond lengths measuring 1.94 Å. A hydrogen ion

(H^+) is bonded in a single-bond geometry to one O^{2-} atom, with a bond length of 0.96 Å. The O^{2-} ion is coordinated in a distorted single bond configuration to four equivalent Li^+ ions and one H^+ ion. To incorporate an adequate concentration of Al, monolayer supercells of 4×4×1 were constructed, allowing

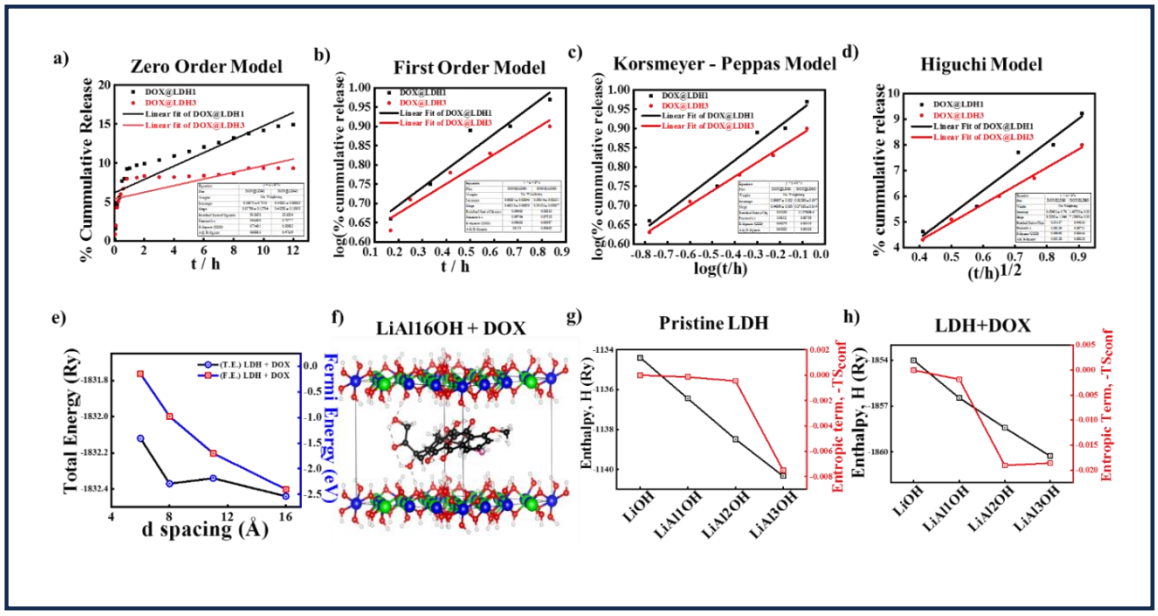

Figure 3.5: Plots of different kinetic models **a)** Zero order model, **b)** First order model, **c)** Korsmeyer-Peppas model and **d)** Higuchi model for the release of DOX from developed DOX@LDH1 and DOX@LDH3 nanoformulation; **e)** Change of total energy and Fermi energy with variation of d-spacing in Li-Al based LDHs and DOX intercalated Li-Al based LDHs nanoformulations; **f)** With much higher Al content in the LDH system (LiAl16OH + DOX), although an increase in stability and interaction with the drug molecule is observed, but the crystal structure is found to be somewhat distorted, with too high Al content. Many dangling bonds are observed in regions with higher density of Al content on the LDH surface, where the limitations of the original lattice size are violated to an extent. Thermodynamics study of **g)** Pristine Li-Al based LDHs, **h)** DOX intercalated Li-Al based LDHs, LDH + DOX. With the increase of aluminium doping into the lithium hydroxide

crystal, the thermodynamics results reflects the stability of nanocarriers (Li-Al based nanocarriers) and nanoformulations (i.e. better interaction between DOX and nanocarriers).

for increased interlayer spacing to accommodate the DOX molecule. The optimization of the entire LDH-DOX system was performed across varying interlayer distances of 6, 7, 8, and 10 Å **(Figure. 3.5.e**) to evaluate the stability and interaction between the two systems, focusing on the 8 Å spacing that aligns with experimental observations. At this interlayer distance, the intercalated system displayed significant stability, exhibiting the lowest ground state total energy during relaxation calculations. Al^{3+} doping in the LiOH 4×4 supercells was limited to less than 10% to maintain uniform bond distribution and prevent structural distortion. To ensure charge neutrality in experimental conditions, the LDH portion was maintained with a net positive charge, typically balanced by nitrate or chloride ions. Given the computational challenges of modelling such large systems, external anions were excluded, assuming that additional electrons stem from the drug molecule. As illustrated in **Figure. 3.4.d**, the DOX molecule, comprised of C, H, N, and O atoms, spans approximately 15 Å in length and 11 Å in breadth, positioning itself nearly parallel to the LDH sheet due to intermolecular attractions among adjacent O and H atoms, thus forming a stable confined system. Strong hydrogen bonds were observed, confirming a robust intercalated structure in the LDH-DOX system, which facilitates a slow and controlled drug delivery.

Both stability and intercalation capability of DOX improve with increased Al concentration, as compared to the pure LiOH + DOX intercalated system, and indicated by a gradual reduction in total energy (**Figure. 3.4.e**). It is evident that the conformation of DOX changes within the LDH matrix as Al content increases, leading to a more stable conformation with a lower ground state energy than that of the pristine DOX molecule (**Figure. 3.4.f**). Additional evidence of stronger interactions is provided by the reduction in

hydrogen bond lengths between the oxygen in DOX and hydrogen in the LDH system, which decreases systematically with rising Al content (**Figure. 3.4.g**) (LiAl1OH→1.87 Å, LiAl2OH→1.73 Å, and LiAl3OH→1.65 Å). Consequently, higher Al concentrations in LDH (such as in LDH3 / DOX@LDH3) effectively regulate the drug's mobility and uptake, enhancing their efficiency as delivery vehicles.

When Al doping exceeds 15%, the crystal structure shows some distortion, although enhanced stability and interaction with the drug molecule are still noted. In areas with higher Al densities, many dangling bonds appear, suggesting that the limitations of the original lattice are somewhat exceeded. To ensure accurate assessments of drug interactions, the focus remains on systems with Al doping below 10%, where the conformational and structural integrity is maintained. From a thermodynamic standpoint, the free energy of a system is influenced by its enthalpy (H) and entropy (S), as described by the Gibbs free energy relation, G = H – TS, where T represents the system's temperature. Relaxation calculations for intercalated systems indicate that the total energy, F, includes contributions from one-electron, Hartree, exchange correlation, and Ewald terms, expressed as F = E - TS, where E is the system's internal energy. The thermodynamic properties significantly affect both the stability and mobility of the drug within the carrier. The system demonstrates a high negative enthalpy and entropy value from smearing contributions (-TS conf.), leading to a net negative free energy in **Figure.3.5 (g,h),** thereby making the LDH-drug intercalation process spontaneous. Experimental and theoretical analyses both indicate enhanced uptake and sustained release from varying dimensions of LDHs, along with suitable mechanisms.

3.2.4 Biocompatibility of nanocarriers along with *in vitro* cell killing efficiency of DOX loaded nanovehicles

Biocompatibility is a critical parameter often assessed via *in vitro* cell viability studies. In this investigation, Li-Al-based LDHs were evaluated as potential drug delivery systems for tumor therapy using the MTT assay to determine SiHa cell viability across different time points. The assay, which relies on the NADPH enzyme activity in living cells, transforms MTT into purple-colored formazan crystals. After 72 hours of incubation, the Li-Al-based LDH nanocarriers demonstrated nearly 100% cell viability, confirming their suitability for drug delivery and biological applications in **Figure. 3.6(a,b,c)** that presents also fluorescence images that reveal increased cell density and proliferation rates, indicative of their biocompatibility. Quantitative assessment of optical density further supports the biocompatible nature of these nanocarriers. Cell morphology on nanocarriers (LDH1, LDH2, and LDH3) without the drug showed flat, well-spread, and elongated forms, with enhanced cell-to-cell contacts, marking them as favourable biomaterials. The percentage of cell adhesion was found to be 87±1.5, 88±1.6, and 89±1.3% for LDH1, LDH2, and LDH3 nanocarriers, respectively in **Figure 3.6(d,e**).

The effectiveness of the DOX-loaded formulations was also evaluated through fluorescence imaging of SiHa cells stained with acridine orange (AO) and ethidium bromide (EtBr) to visualize the induction of apoptosis (**Figure.3.7.a**). The selective membrane permeability for different stains allows for the differentiation between healthy and apoptotic cells, where AO binds to DNA and fluoresces green, while EtBr is taken up by apoptotic cells, resulting in red fluorescence from condensed nuclei. Cells stained with AO/EtBr exhibit yellow-orange and red fluorescence for apoptotic and necrotic cells, respectively, while viable cells emit green fluorescence. The DOX-loaded LDHs (DOX@LDH1 and DOX@LDH3) demonstrated a combination of live and apoptotic cells, contrasting with the predominance of live cells observed with the control and pure DOX. Notably, DOX@LDH3 showed a higher proportion of apoptotic cells, highlighting its

enhanced antitumor activity, consistent with the time-dependent MTT assay results (**Figure.3.7.b**).

The efficiency of the controlled drug release from these nanocarriers was assessed by comparing their cancer cell-killing efficacy. At a concentration of 20 µg/ml, DOX@LDH1 and DOX@LDH3 resulted in SiHa cell death rates of 65% and 72%, respectively, compared to a minimal 2% lethality with pure DOX (pH ~7.5-8). The negatively charged DOX struggles to enter cells due to electrostatic repulsion, while the positively charged DOX-loaded LDHs effectively penetrate the cells, leading to apoptosis and necrosis. A continuous decrease in cell viability was observed for the DOX-loaded LDHs over time, whereas a slight increase was noted for the pure drug. Among the LDHs, DOX@LDH3 exhibited the highest cytotoxicity, attributed to its sustained drug delivery characteristics and greater drug uptake due to its larger two-dimensional size. This property allows DOX@LDH3 to minimize frequency of dosing compared to conventional delivery

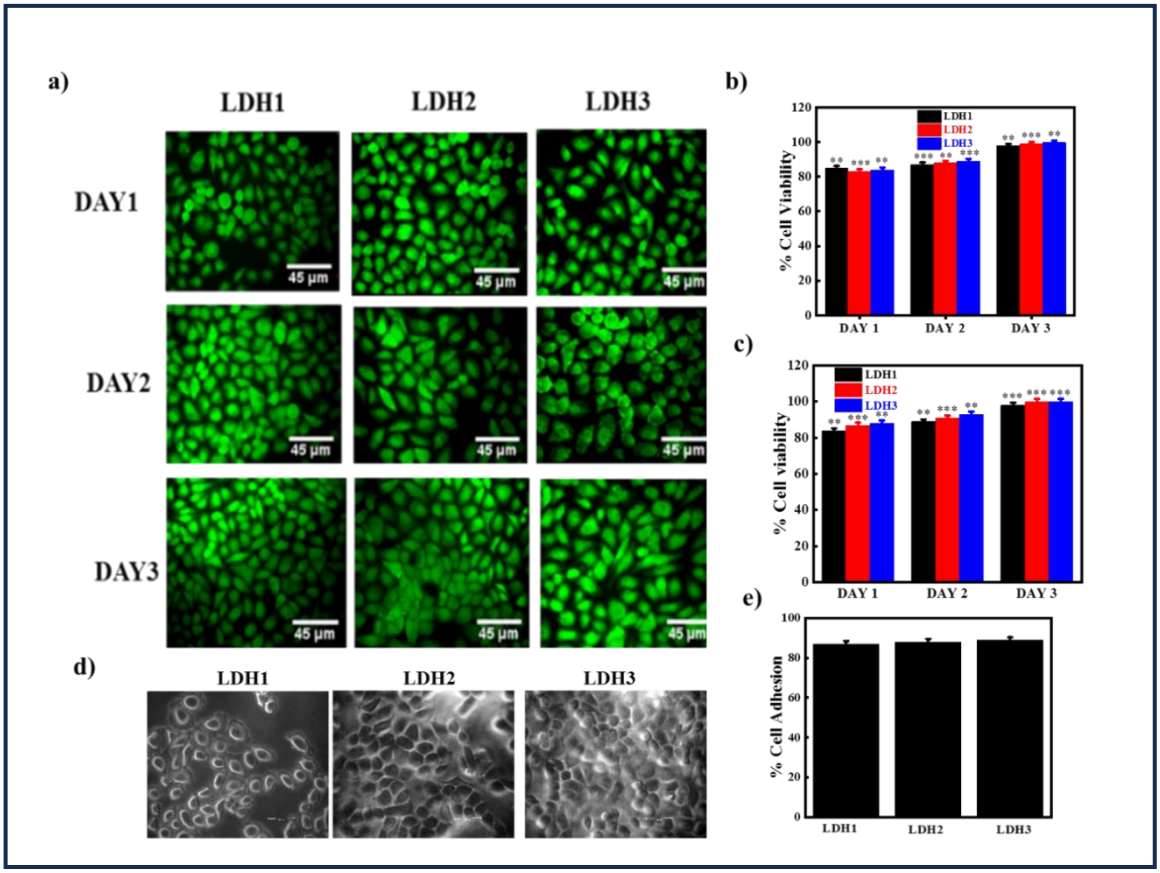

Figure 3.6: a) Fluorescent microscopic images of AO/ EtBr staining of LDH1, LDH2 and LDH3 nanocarriers; b) Cell viability study of LDH1, LDH2 and LDH3 against SiHa cells using MTT assay as a function of time; c) Cell viability of LDH1, LDH2 and LDH3 nanocarriers against 3T3-L1 using MTT assay as a function of time d) Phase contrast images of LDH1, LDH2 and LDH3 nanocarriers; e) Percentage cell adhesion value of LDH1, LDH2 and LDH3 nanocarriers.

methods or pure drug applications. Notably, the failure of pure DOX to maintain effective concentrations for cancer cell lethality is linked to its limited availability over extended periods.

The biocompatibility of the nanovehicles was further evaluated using fibroblast cells (3T3-L1) to assess potential toxicity towards non-cancerous cells. All nanocarriers (LDH1, LDH2, and LDH3) displayed approximately 100% cell viability, confirming their non-toxic In contrast, DOX@LDH1 and DOX@LDH3 exhibited cell viabilities of 48±1.4% and 58±1.6%, respectively, after 72 hours of incubation (**Figure.3.7.c**), indicating a significantly lower viability compared to SiHa cells. Thus, the developed nanoformulations demonstrate a degree of selectivity towards cancer cells over normal cell lines, presenting a promising strategy for tumor treatment, with DOX@LDH3 proving more effective than DOX@LDH1 in terms of cancer cell cytotoxicity and reduced toxicity to normal cells.

To further elucidate the intracellular dynamics of DOX@LDH3, microscopy was utilized to assess the intracellular trafficking. This nanoformulation was shown to enter cells via a clathrin-mediated endocytosis pathway. After one hour of treatment, DOX was observed to colocalize with LysoTracker Green-labelled lysosomes (**Figure.3.7.d**). However, over

prolonged incubation, the colocalization diminished, with DOX primarily localizing in the nucleus after six hours. These findings indicate that DOX@LDH3 is internalized, initially localizes in lysosomes, undergoes degradation in response to acidic lysosomal conditions, and ultimately releases DOX into the nucleus, contributing to its cytotoxic effects.

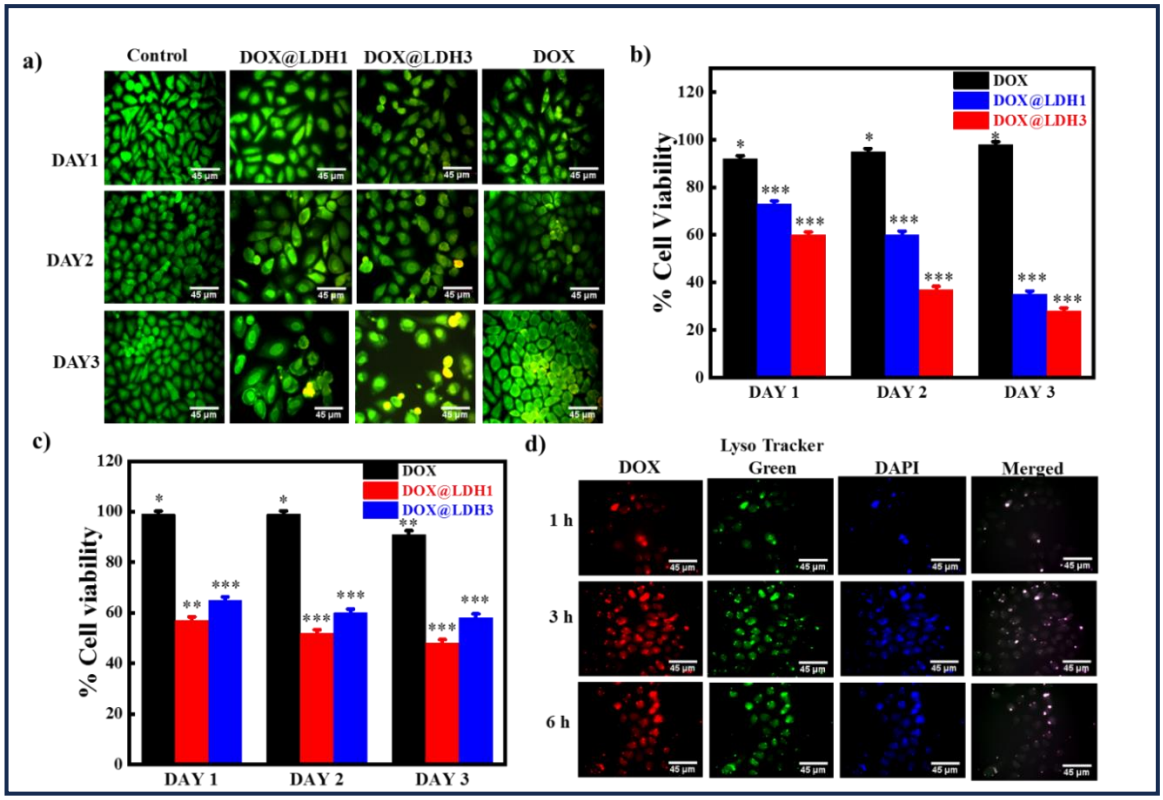

Figure 3.7: Comparison study of biocompatibility and *in vitro* cytotoxicity on cancer cell line (SiHa) and normal cell line (3T3-L1) along with intracellular trafficking using different trackers. **a)** The relative number density of cells following treatment is shown in fluorescent microscopic images of AO/EtBr staining of control, doxorubicin (DOX, pH~7-8), DOX loaded LDHs (DOX@LDH1 and DOX@LDH3) with the concentration of 20 µg/ml. Scale Bar: 45 µm; **b)** MTT assay-based cell viability analysis of DOX, DOX@LDH1 and DOX@LDH3 against SiHa cells line with concentration 20 µg/ml; **c)** DOX, DOX@LDH1 and DOX@LDH3 groups (20 µg/ml) *in vitro* cytotoxicity in 3T3-L1 fibroblast cells at various incubation time intervals: results are shown in mean value ±SD,

n = 3, *** p < 0.001, ** p < 0.01, * p < 0.05; and **d)** Microscopic images of SiHa cells which has been stained with 100 nM LysoTracker green and 5 μg/ml DAPI after being exposed to DOX@LDH3 (20 μg/mL) for indicated time periods. Magnification: 40x.

3.2.5 Controlled cellular uptake along with LDH nanocarrier induced cell adhesion

To truly grasp the impact of biologically active molecules on cells, it is essential to understand how these molecules traverse the cell membrane, journeying from the extracellular space into the cytoplasm. The efficacy of drug molecules in destroying cells is fundamentally tied to their ability to penetrate the cell membrane from the drug delivery system into the cell interior. In this study, DOX-loaded nanocarriers, LDH1 and LDH3, are utilized to assess the relative effectiveness of drug uptake compared to pure DOX (conventional therapy). The cellular uptake study was conducted on the human cervical cancer cell line, SiHa, to elucidate the biological potential of DOX@LDH1 and DOX@LDH3 nanoformulations over time (**Figure.3.8.a**). Significant uptake was observed through fluorescence imaging in both nanoformulations, contrasting sharply with the minimal uptake seen with pure DOX. Notably, DOX@LDH1 exhibited a rapid uptake, likely due to the smaller particle size of LDH1, while DOX@LDH3 showed sustained uptake, consistent with its drug release profile. A time-dependent increase in uptake, reflected by mean fluorescence intensity, is presented in **Figure.3.8.b**, showing a steady rise for both formulations, while pure DOX exhibited only negligible uptake over the same extended period. It is important to note that negatively charged DOX alone is unable to effectively penetrate the cell membrane. However, when embedded within positively charged LDHs, DOX can easily cross the membrane, enhancing cellular uptake. Furthermore, the varying sizes of LDH can modulate uptake based on the drug's intracellular requirements through the process of endocytosis. Research by Choy et al.

demonstrated that clathrin-mediated endocytosis is the primary mechanism behind the efficient uptake of LDH nanoparticles, with an upper size limit of 200 nm for lateral dimensions. This supports the conclusion that the larger LDH3 nanocarrier successfully facilitates DOX transport into the cell. Two key stages explain the cellular absorption of LDHs and DOX-loaded LDHs: the initial adhesion of LDHs to the cell surface, followed by interactions with cell membrane lipids and proteins, which promote an energy-dependent uptake mechanism. The effectiveness of cellular absorption increases in parallel with adherence, a critical step in determining the biocompatibility of a material. Cells must adhere to a surface before they can proliferate. Li-Al-based LDH nanocarriers and their nanoformulations were evaluated both qualitatively, based on their morphological characteristics, and quantitatively, by measuring optical density to assess cell viability. In contrast, DOX@LDH1 and DOX@LDH3 induced a contracted morphology with reduced cell-to-cell contact, primarily due to DOX's cell-killing action (**Figure.3.8.c**), yielding viable cell percentages of 80±1.9% and 68±1.3%, respectively, which demonstrates their efficacy as potent nanocarriers (**Figure.3.8.d**). However, the nanocarriers themselves exhibited superior cell adhesion, likely due to their hydrophilic properties, which enable cells to fully spread across their surface. This, in turn, promotes considerable cellular uptake by facilitating the delivery of drug-loaded LDHs into the cytoplasm via endocytosis, resulting in enhanced cell-killing efficiency.

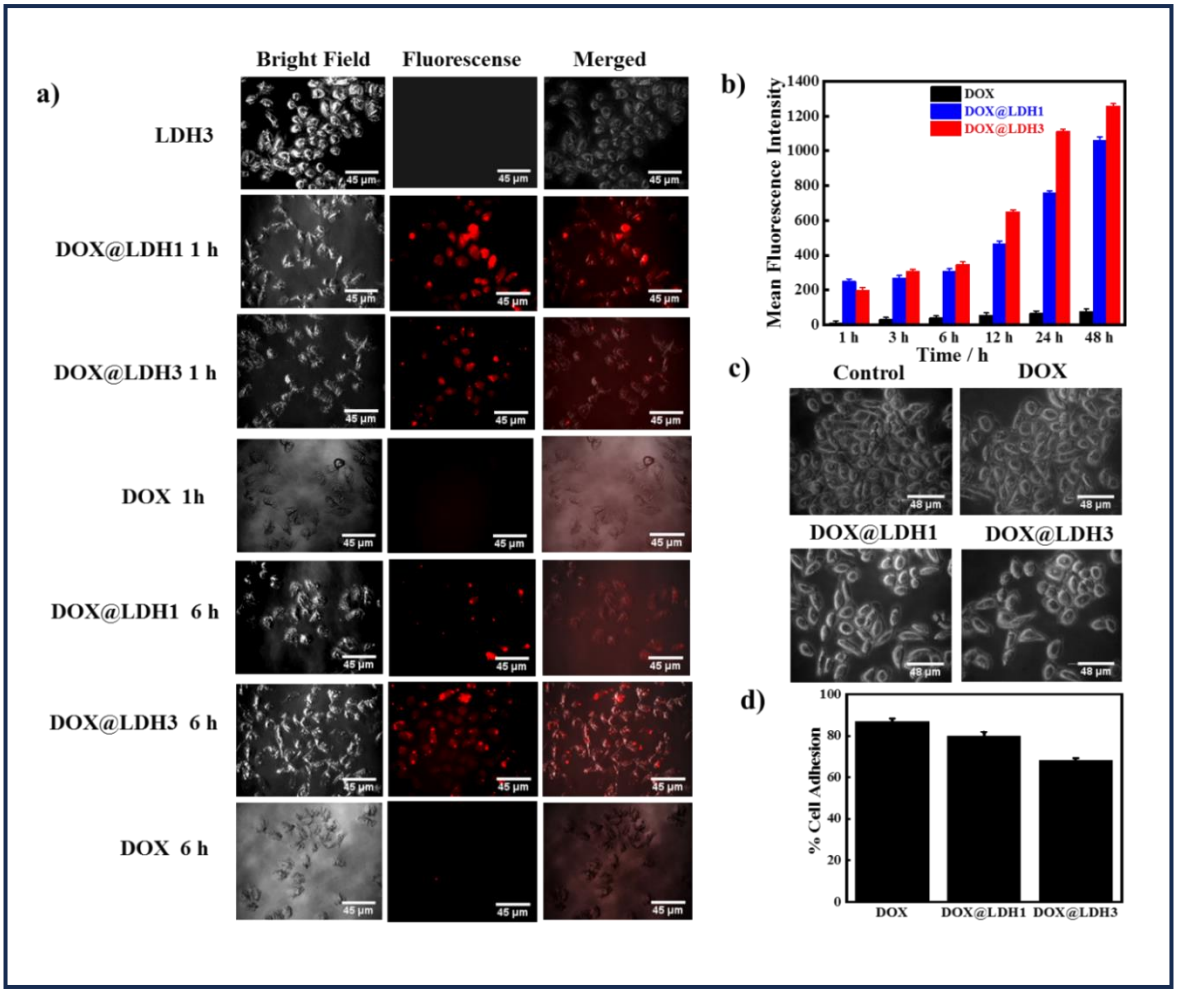

Figure 3.8: *In vitro* cellular characterization of DOX loaded Li-Al based LDHs nanoformulations, capacity on uptake and adherence properties in cancer cell line (SiHa); **a)** Fluorescence microscopic images demonstrating how SiHa cells ingest DOX loaded LDH1and LDH3 (DOX@LDH1and DOX@LDH3) with time. LDH does not exhibit any fluorescence. Depending on cellular absorption, cells are exposed to 20 µg/ml DOX, pristine LDH (LDH3) and DOX loaded nanoformulations that exhibit varying fluorescence intensities. Magnification: 40x; **b)** Cellular uptake kinetics analysis using SiHa cells under various incubation periods. DOX was penetrated into the cells in the presence of DOX@LDH1 / DOX@LDH3 with equivalent DOX concentration of 20 µg/ml; **c)** Phase contrast images of the SiHa cells grown on the indicated substrates after 24 hours of

incubation, scale bar: 48 μm; and **d)** The relative cell adhesion values after 24 hours of incubation using the designed indicated nanoformulations.

3.2.6 In vitro apoptotic mechanistic pathway using nanoformulation

This study investigates the apoptotic mechanisms triggered by doxorubicin (DOX) in SiHa human cervical cancer cells, utilizing nanoformulations (DOX@LDH1 and DOX@LDH3) to enhance drug efficacy. Flow cytometry, an efficient method for assessing cell viability and cell cycle distribution, was employed, leveraging fluorescent dyes such as Propidium iodide (PI) to analyze cell cycle phases. The treatment of SiHa cells with DOX, DOX@LDH1, and DOX@LDH3 at a concentration of 20 μg/ml led to significant G2/M phase arrest. Specifically, the percentages of apoptotic cells were quantified as 9.2%, 32.4%, and 52.5%, respectively, reflecting an increase in apoptosis correlated with the nanoformulation (**Figure 3.9.a**). Key indicators of apoptosis, including nuclear condensation, plasma membrane blebbing, nuclear fragmentation, and a characteristic 200 base pair DNA laddering due to internucleosomal DNA degradation, were observed. Notably, the integrity of mitochondrial function and membrane integrity remained intact prior to the onset of apoptosis [51].

During apoptosis, the phospholipid asymmetry of the cellular membrane is disrupted, leading to the translocation of phosphatidylserine from the inner to the outer leaflet. This early event in the apoptotic process is critical for distinguishing between early apoptotic and late apoptotic/necrotic cells using flow cytometry. The Annexin V/PI staining assay differentiates these populations effectively. The percentages of necrotic and late apoptotic cells for DOX, DOX@LDH1, and DOX@LDH3 were determined to be 21/1.9, 12.7/87.2, and 37.7/61.9, respectively, indicating a shift towards necrosis particularly with DOX@LDH3, which also exhibited sustained drug release properties (**Figure 3.9.b**).

Apoptosis induced by anti-proliferative drugs may be mediated through either death receptor-dependent pathways or mitochondrial-dependent pathways. A schematic representation of the sustained drug delivery mechanism and the sequence of apoptotic events in response to these nanoformulations is presented in **Figure 3.9.c**. Understanding the expression of specific apoptotic proteins is essential for elucidating the underlying mechanisms of apoptosis. Our results indicated that treatment with DOX and DOX@LDH3 significantly activated caspases 3, 6, and 7, pivotal in the apoptotic execution phase. The cleavage of pro-caspase-3 to its active form was markedly enhanced by DOX and DOX@LDH3, with fold changes of 0.72, 0.96, and 0.85, respectively (**Figure 3.9.d**). Furthermore, the cleavage of PARP (116 kDa) into an 89 kDa fragment confirmed the activation of caspase-3, serving as a hallmark of apoptosis. The BCL-XL family of proteins plays a critical role in regulating the intrinsic apoptotic pathway. Overexpression of anti-apoptotic proteins like BCL-XL can reduce the effectiveness of chemotherapeutic agents. Our findings suggest that DOX@LDH3 may be more effective than DOX and DOX@LDH1 in lowering BCL-XL expression, with fold changes of 0.64 and 0.75, respectively. This implies that the intrinsic pathway is likely the primary mechanism through which DOX@LDH3 induces apoptosis in SiHa cells. Activation of the tumor suppressor protein p53, known for its role in mediating cell cycle arrest and apoptosis, was also observed. Under cellular stress, p53 promotes the expression of genes involved in G1 or G2/M arrest, such as p21Waf1. Our experimental data reveal that the designed nanoformulation, DOX@LDH3, significantly enhances G2/M phase arrest, corresponding with increased p53 expression compared to pure DOX and other formulations. The activation of p53, particularly through phosphorylation at Ser15, is crucial for its transactivation capabilities and stability, further underscoring the potential of our nanoformulation in enhancing therapeutic efficacy against cervical cancer cells.

In conclusion, the findings indicate that DOX@LDH3 not only enhances the induction of apoptosis but also promotes cell cycle arrest in SiHa cells, showcasing its potential as an effective therapeutic strategy in cancer treatment. Further investigations into the detailed mechanisms at the molecular level are warranted to fully understand the implications of these results.

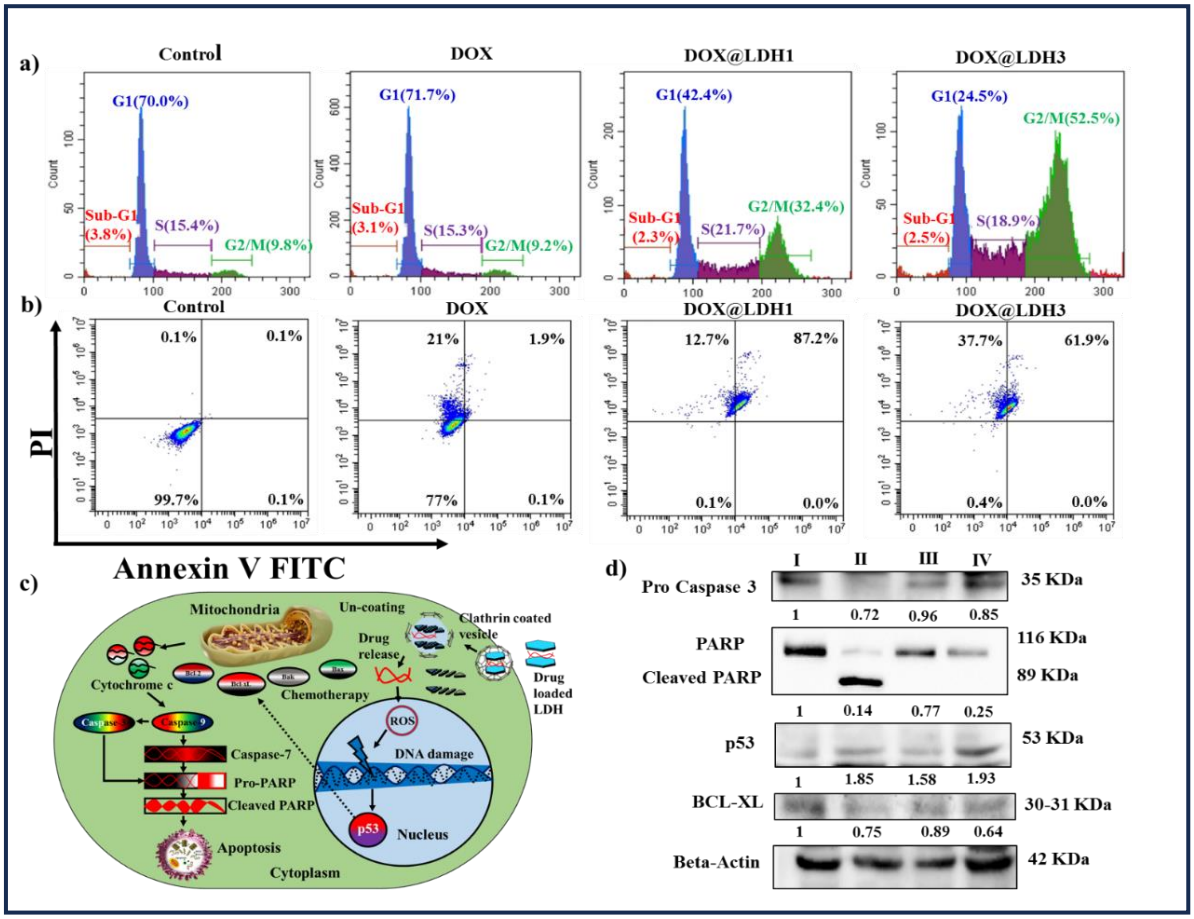

Figure 3.9: *In vitro* evaluation on the antitumor effect of the designed nanoformulations. **a)** Cell cycles were arrested following the treatment with three distinct chemotherapeutic agents. SiHa cells were either left untreated (control), or were given DOX, DOX@LDH1 and DOX@LDH3 (20 µg/ml) for 24 hours. The cells were fixed and stained with propidium iodide to detect DNA. The percentages of cells in G1, S, and G2/M states were determined using CytExpert Software; **b)** SiHa cells exposed to DOX, DOX@LDH1 and DOX@LDH3 had their annexin V and propidium iodide staining examined through flow cytometry. Control and three groups (20 µg/ml) were administered to cells for 24 hours.

Propidium iodide (PI) labelled population is stained on the y-axis while Annexin V-FITC binding is seen on the x-axis. Viable cells are found in the lower left quadrant and are Annexin V negative and PI negative, early apoptotic cells are found in the lower right quadrant and are Annexin V positive and PI negative, and necrotic and late apoptotic cells are found in the upper left and right quadrant, respectively; **c)** The suggested molecular mechanism for the apoptotic cell death caused by nanoformulation; and **d)** Western blot analysis of SiHa cells after the treatment of PBS (I), DOX (II), DOX@LDH1 (III) and DOX@LDH3 (IV) (20 μg/ml) for 24 h, to determine the expression of Pro-caspase 3, BCL-XL, p53 and PARP proteins. Proteins from cell lysates were produced, separated on SDS-polyacrylamide gel, and then transferred to nitrocellulose membranes. The indicated antibodies were used to probe the membranes. Protein loading was monitored using β-actin as control. The findings presented here arise from two or three separate investigations.

In a recent study utilizing Western blot analysis, we examined the phosphorylation of p53 at Ser15 using a specific antibody. Our results demonstrated a time-dependent increase in phosphorylated p53 following administration of doxorubicin (DOX). Elevated levels of p53 have been associated with impairments in long-term potentiation (LTP), which plays a critical role in learning and memory, as well as the effects of aging and oxidative stress. While p53 is typically found in low levels in healthy cells, its expression is markedly increased in various transformed cell lines, suggesting its involvement in malignancy. This is supported by our findings, which indicated a fold change of 1.93 for the DOX@LDH3 nanoformulation compared to a fold change of 1.85 for DOX alone (**Figure.3.9.d**) [52]. These results suggest that the developed nanoformulation, DOX@LDH3, is effective in modulating biomolecular processes relevant to tumor treatment, warranting further investigation in animal models.

3.2.7 Molecular Docking Analysis

We conducted a theoretical molecular docking analysis to explore the binding interactions between DOX and the DNA receptor, DNA topoisomerase II alpha. The interaction was characterized by a favourable binding energy of -8.9 kcal/mol (see supplementary Fig. S8b). The docking studies further identified the specific binding sites, hydrogen and oxygen bonds, and the involved amino acid residues (**Table 3.2**). The DOX-loaded LDH nanocarriers facilitate the delivery of DOX into cells, particularly targeting the nucleus. This interaction with DNA topoisomerase II alpha results in the over winding of DNA during transcription and inhibits DNA double strand recombination, effectively halting DNA replication.

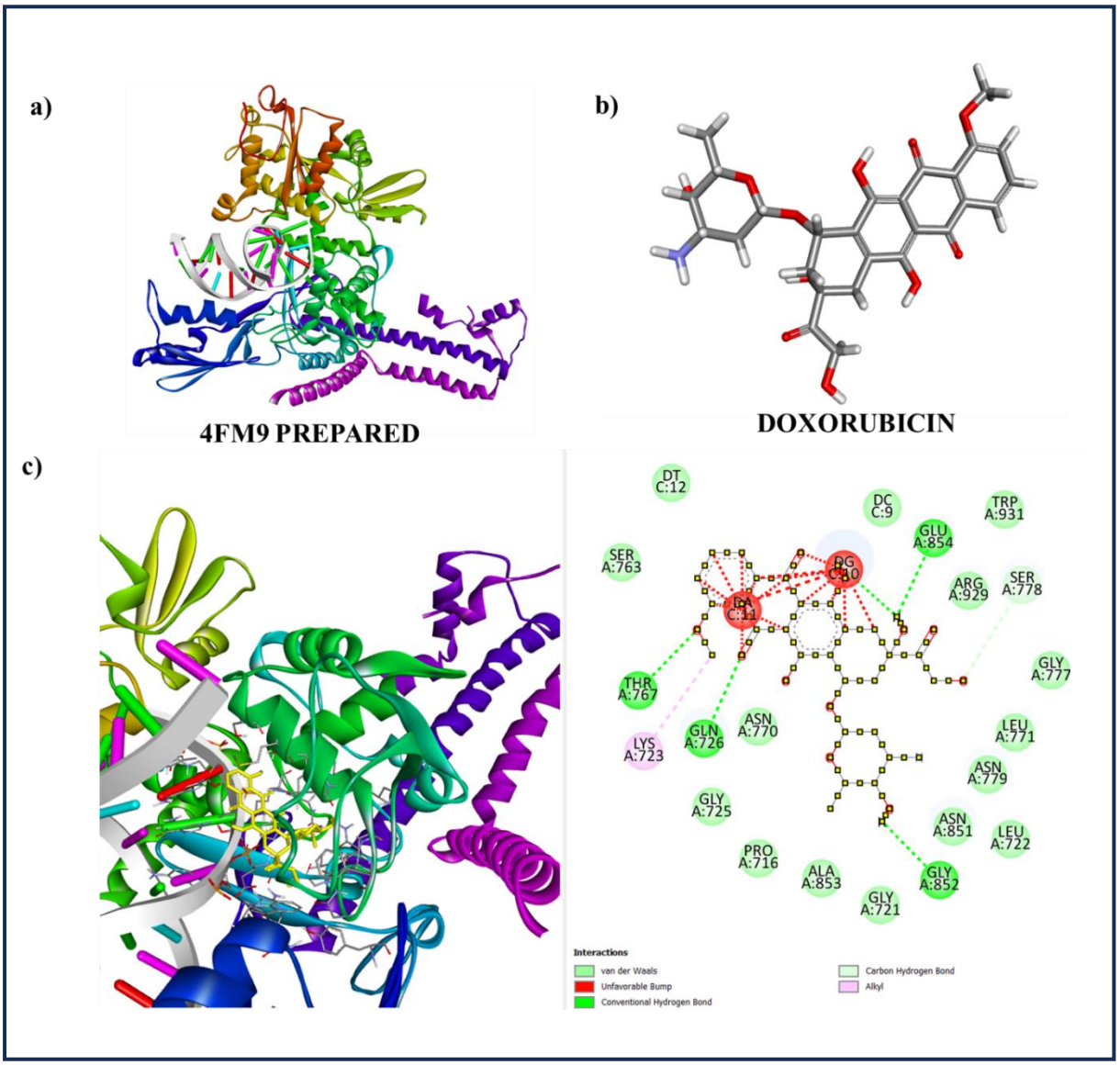

Figure 3.10: a) 3D view of receptor DNA topoisomerase II alpha. PDB (PROTEIN DATA BANK) ID-4FM9 (https://www.rcsb.org/structure/4fm9). The X-ray crystal structure DNA topoisomerase II alpha was retrieved from the RCSB PDB database. The obtained crystal structure of the receptor was prepared for receptor- ligand docking by following steps: water molecules, bound atoms were removed by using of widely used visualization tool-BIOVIA DISCOVERY STUDIO (2021). The energy was minimized by the PyRx software; **b)** Chemical structure of doxorubicin drug as a ligand PubChem ID-31703 (https://pubchem.ncbi.nlm.nih.gov/compound/Doxorubicin). The three dimensional (3D) structure of Doxorubicin retrieved from PubChem as SDF format; **c)** 3D view of Doxorubicin- DNA complex along with different type of interaction between ligand and receptor. The molecular docking of doxorubicin molecule with the receptor DNA topoisomerase II alpha was performed with the aid of PyRx software. After preparation of receptor (PDB ID-4FM9) and respective ligand (doxorubicin) molecule were uploaded on PyRx. After successful uploading, molecular docking has performed followed by the docking process of the software. After completion of docking process best docking results has obtained which pose in the receptor cavities.

SR.NO	Ligand	PuBChem ID	Receptor	PDB ID	Binding energy (kcal/ mol)	Total Bonds	Reacting Amino acids /nucleotide residues of receptor with position	Reacting atoms of ligand	Distance (Å)
1.	Doxorubicin	31703	DNA topoisomerase 2 alpha	4FM9	-8.9	8	THR-767	O	2.4
							GLN-726	O	2.3
							GLN-726	O	2.6
							GLY-852	H	2.3
							GLU-854	H	2.4
							ARG-929	O	2.6
							DG-10	O	3.3
							DG-10	H	1.7

Table 3.2: Molecular docking analysis to determine the binding sites, interacting hydrogen and oxygen bonds, amino acid residues and atoms. PyRx was used for calculating the docking score and root mean square deviation (RMSD) values of interacting molecules. The binding site and interaction were visualized by virtual screening tool Pymol software. Using Pymol software; bonds, distance between bonds, and interacting amino acid/ nucleotides residues were estimated for ligand molecule. Receptor- ligand interaction and generation of images were rendered using Pymol AND BIOVIA DISCOVERY STUDIO-2021 (DeLano, 2002). The best-suited conformations with the lowest root mean square deviation (RMSD) values, highest docking score, and number of amino acids residues with binding H and O bonds were collected.

3.2.8 *In Vivo* Tumor Study Using a Melanoma Mouse Model

To assess the efficacy of a sustained drug release system in treating melanoma, we employed an injectable hydrogel delivery method. We generated palpable tumors in mice, using the B16-F10 cell line, which resulted in tumors averaging 50±10 mm^3 in volume. We formulated an injectable methyl cellulose (MC) hydrogel, chosen for its biocompatibility

and gel-forming properties, to ensure prolonged contact with the tumor site. The rheological properties of MC were validated through both the inversion test tube method and *in vivo* assessments. **Figure 3.11.a** illustrates the therapeutic approach of the injectable hydrogel embedding the novel DOX@LDH3 nanoformulation, injected just beneath the tumor for optimal drug retention and permeation.

Mice with melanoma were randomly assigned to three treatment groups: a saline control, DOX in MC (DOX-MC), and DOX@LDH3 in MC (DOX@LDH3-MC). All groups received the same dosage of DOX. Notably, the tumor volume in the DOX@LDH3-MC group significantly decreased over time, reaching a relative volume of 4.6 mm^3 after 27 days (Fig. 7b), while control mice exhibited a steady increase in tumor volume (relative volume 260±20 mm^3). Quantitative analysis revealed that the DOX@LDH3-MC group achieved significant tumor reduction, whereas the DOX-MC treatment led to minimal suppression compared to controls (**Figure.3.11.c**).

The sustained drug release from the DOX@LDH3-MC system maintains therapeutic concentrations at the tumor periphery for an extended period. In contrast, the rapid release profile of DOX-MC results in a quick surge of DOX into the bloodstream, leading to diminished bioavailability and effectiveness over time. Consequently, mice treated with DOX-MC showed minimal tumor control. Additionally, mice receiving DOX@LDH3-MC experienced slower weight gain, indicating fewer side effects, while the DOX-MC group exhibited significant weight increase, primarily due to tumor growth (**Figure 3.11.d**).

The DOX@LDH3 nanoformulation allows for prolonged drug delivery, keeping plasma concentrations within a therapeutic range for an extended duration, thus mitigating adverse effects commonly associated with conventional DOX treatments. To evaluate the pharmacokinetic profiles of the treatments, we measured drug concentrations in the

bloodstream following intravenous administration of 5 mg/kg of DOX, DOX@LDH1, and DOX@LDH3. The concentration of DOX in the pristine solution peaked rapidly (C_{max} = 9.15 µg/ml) within six hours and fell below the minimum inhibitory concentration (MIC) against Mycobacterium smegmatis (Msm) [53] within twelve hours (**Figure.3.11.e**). Conversely, both DOX@LDH1 and DOX@LDH3 demonstrated sustained release, maintaining concentrations above the MIC for up to 40 hours, particularly with DOX@LDH3, indicating an effective and prolonged delivery from the nanocarriers. This study suggests that larger two-dimensional LDH nanocarriers (~150 nm) represent an optimal strategy for controlled drug delivery, minimizing the risk of rapid concentration spikes and associated side effects in tumor therapy.

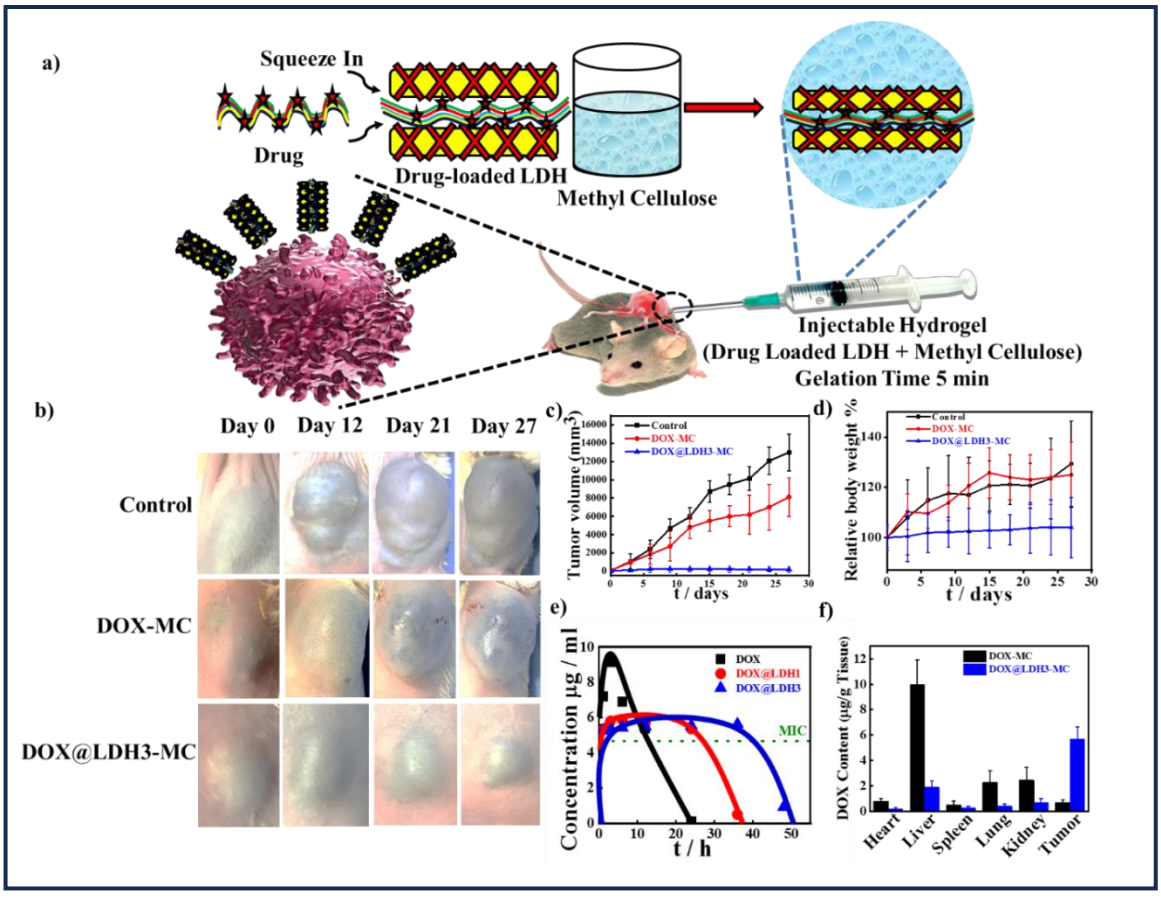

Figure 3.11: *In vivo* therapeutic efficacy of the nanoformulation using melanoma bearing mice**. a)** Schematic illustration of apoptosis based therapeutic action of DOX@LDH3-MC.

The injectable hydrogel was injected just below the tumor site, DOX would be accumulated in tumor tissues due to the enhanced permeability and retention effect; **b)** Images taken of the tumor size in mice before and after treatments with DOX-MC (DOX in MC gel), DOX@LDH3-MC (DOX embedded in LDH3 and further embedded in MC gel), and control (only saline); **c)** Measured tumor volume as a function of time following the therapy with various approaches, as appropriate; **d)** Percentage of relative body weight as a function of treatment time in each group; **e)** Following intravenous administration of either pure DOX (5 mg/kg of mice weight) or DOX intercalated LDH1 and LDH3 (DOX@LDH1 and DOX@LDH3) with an equivalent quantity of drug in dispersion condition, the drug concentration profile in plasma was determined as a function of time. The dotted line represents the minimum inhibitory concentration (MIC) of DOX for Mycobacterium smegmatis (M_{sm}); and **f)** The concentration of DOX in tumor tissue and different organs from melanoma tumor-bearing mice treated with DOX-MC or DOX@LDH3-MC at a dose of 5 mg/kg after 72 hours of injection.

The *in vivo* findings indicate that DOX@LDH3 serves as an effective drug carrier for sustained release, making it a suitable option for melanoma treatment. The comparative analysis of doxorubicin (DOX) accumulation in tumors across different treatment modalities provides insights into the efficacy of the nanovehicle relative to conventional DOX therapy. The concentrations of DOX in tumors treated with DOX-MC and DOX@LDH3-MC were measured at 0.7 μg/g and 5.7 μg/g of tissue, respectively, demonstrating a significantly improved biodistribution for the DOX@LDH3-MC formulation in melanoma-bearing mice (**Figure.3.11.f**). This enhanced distribution is likely attributed to the positive surface charge of the nanovehicle, contrasting with the negative charge of pure DOX.

Moreover, analysis of DOX levels in vital organs such as the heart, liver, spleen, kidneys, and lungs revealed lower concentrations in the DOX@LDH3-treated mice compared to those receiving pure DOX. Notably, the concentration of DOX in the liver was markedly higher in mice treated with the DOX-MC formulation, which raises concerns regarding potential side effects associated with higher liver concentrations. This observation underscores the advantages of using nanovehicles for safer tumor treatment.

3.2.9 Histopathological and Immunohistopathological Analyses

To assess the potential impact of sustained drug release on other organs during tumor treatment, we performed histopathological evaluations. Hematoxylin and eosin (H&E) staining was conducted on critical organs, including the liver, spleen, and tumor tissues, post-treatment to determine toxicity levels associated with both the pure drug and drug-intercalated systems. The control group exhibited significant necrosis and nuclear shrinkage at the tumor interface, characterized by minimal lymphocytic infiltration and extensive necrosis (**Figure.3.11.a**). Conversely, the pure DOX-treated group showed mild to moderate lymphocyte infiltration and smaller necrotic areas, while the DOX@LDH3-MC group demonstrated a dense lymphocytic presence alongside larger necrotic areas, indicating enhanced anti-tumor activity.

The Li-Al based LDH nanocarrier displayed effective anti-cancer properties through its sustained release mechanism, corroborated by histological findings. Importantly, the liver architecture remained normal in mice treated with DOX@LDH3-MC, contrasting sharply with the severe inflammation and distorted hepatocyte structure observed in the control and DOX-MC groups (**Figure.3.11.b**). The spleen tissue showed no apparent damage across all treatment groups.

These results suggest that DOX-MC could induce significant side effects due to rapid drug release, adversely affecting vital organs with minimal anti-tumor efficacy. In contrast, the injectable DOX@LDH3-MC formulation maintains therapeutic concentrations over an extended period, demonstrating a slow, steady release profile with substantial anti-tumor effects while avoiding negative impacts on essential organs. The benefits of the DOX@LDH3-MC formulation stem from its continuous release of the drug, which sustains bioavailability and contributes to tumor shrinkage, ultimately leading to enhanced overall tumor inhibition.

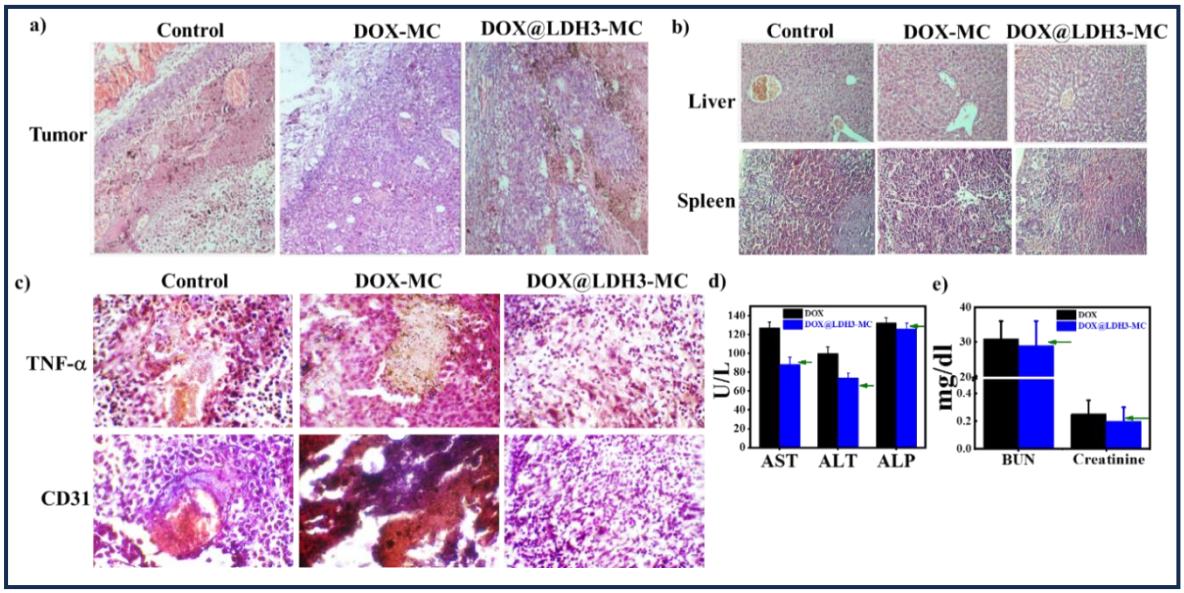

Figure 3.12: Underlying effects of *in vivo* controlled drug release on organs and melanoma tumor along with pharmacokinetic study. **a)** Mice tumor tissue were removed after 27 days of treatment and were subjected to histopathological examination using H&E staining at 100× magnification; **b)** Mice vital organs such as the liver, spleen was collected after 27 days of treatment and were subjected to histopathological examination using H&E staining at 100× magnification; **c)** The immunohistochemistry study of the tissues of the tumor at the end of the treatment process after staining with inflammatory marker (TNF-α) and vascular differentiation marker (CD31) at 40x. **d)** Liver function tests are performed by

comparing the serum levels of AST, ALT, and ALP in various treatment groups; **e)** BUN and creatinine levels in the serum were measured for various therapy groups as part of a renal function test. The arrows indicate the values correspond to the healthy mouse.

Immunohistochemical staining (**Figure.3.11.c**) assessed the expression levels of TNF-α and CD31 across all treatment groups. In the DOX@LDH3-MC group, TNF-α expression was nearly undetectable by the conclusion of the experiment, contrasting with notable levels in both the control and DOX treatment groups. This indicates that not only does inflammation diminish with DOX@LDH3-MC, but also that angiogenesis and granulation tissue formation are significantly enhanced relative to other groups, facilitating accelerated healing in the formulation group. This provides compelling evidence that the drug-loaded LDH formulation (DOX@LDH3-MC) can effectively promote tumor healing in mice.

CD31, a well-known marker for vascular lesions, displayed a higher expression indicative of aggressive tumor behavior in both the control and DOX groups, whereas it was absent in the DOX@LDH3-MC group. This suggests that the latter formulation may be particularly potent for melanoma treatment. Furthermore, histological images revealed significant tumor cell death in the DOX@LDH3-MC group compared to those treated with DOX-MC.

To evaluate potential side effects associated with DOX treatment, liver and kidney function tests were conducted. Key indicators of liver health, namely the enzymes alanine aminotransferase (ALT) and aspartate aminotransferase (AST), were measured. The DOX@LDH3-MC treated group exhibited enzyme levels similar to those of healthy controls (ALT ~ 74 ± 5 U/L, AST ~ 88 ± 8 U/L) (**Figure.3.11.d**). In contrast, the DOX-MC group showed significant elevations in these enzymes (ALT ~ 100 ± 7 U/L and AST ~ 127

± 6 U/L), indicating severe hepatic damage after 27 days of treatment. These results reinforce the safety of the DOX@LDH3-MC formulation in cancer therapy.

Additionally, renal function assessments revealed that mice receiving DOX@LDH3-MC maintained blood urea nitrogen and creatinine levels within the normal ranges (29 mg/dL and 0.2 mg/dL, respectively), while those treated with DOX-MC displayed slightly elevated levels (31 mg/dL for blood urea nitrogen and 0.25 mg/dL for creatinine), suggesting potential renal impairment (**Figure.3.11.e**) [54].

By modifying the elemental composition of Li-Al based LDHs, we developed drug nanocarriers that effectively control drug uptake efficiency and sustain drug release. The architecture of these nanocarriers facilitates diverse interactions, enhancing biocompatibility and minimizing toxicity, thus achieving superior anti-tumor efficacy without the adverse effects commonly seen with traditional therapies.

3.3 Conclusion:

We synthesized Li-Al based LDHs with varying aluminium substitution to optimize their size (approximately 150 nm) and stability. The higher aluminium content allows for increased drug intercalation through ion exchange, resulting in sustained drug release due to the enhanced interactions between the LDH and the drug (DOX). Spectroscopic analysis and density functional theory (DFT) calculations indicate strong interactions, evidenced by shifts in peak positions and reduced energy levels associated with hydrogen bonding. The embedding of negatively charged DOX into the positively charged LDH matrix enhances cellular uptake through negatively charged cell membranes. Notably, drug-embedded LDHs demonstrated a remarkable 72% cell killing efficiency over three days, supported by fluorescence imaging that showed superior cellular uptake compared to pure DOX, which exhibited only a 2% killing rate. Flow cytometric analyses further confirmed a significantly

higher rate of apoptosis in cells treated with the LDH formulation compared to those treated with pure DOX. Mechanistic studies indicated the involvement of various proteins, including caspase 3, p53, and BCL-XL, in the apoptotic process. *In vivo* experiments conducted on melanoma-bearing mice demonstrated a marked reduction in tumor volume with the injectable hydrogel formulation, whereas pure DOX resulted in minimal volume reduction under similar conditions. This disparity can be attributed to the prolonged release of DOX from the LDH system compared to the rapid release associated with pure DOX, corroborated by biodistribution studies showing increased DOX concentrations in tumor tissues from the formulation. Histopathological evaluations indicated improved tumor healing with the nanocarrier, contrasting with the mild lymphocytic infiltrate and necrosis observed in pure drug-treated mice. The healthy liver condition in mice treated with DOX@LDH3-MC versus the significant liver inflammation and hepatocyte damage noted in pure DOX-treated animals suggests that the developed formulation mitigates the adverse effects commonly associated with conventional chemotherapy. Furthermore, immunohistochemical studies aligned with these findings, supporting the beneficial impact of the new LDH-based drug carrier on tumor healing without evident side effects, thereby addressing the limitations of traditional anticancer therapies.

3.4. References

1) Hubbell, J. A., & Chilkoti, A. (2012). Nanomaterials for drug delivery. *Science*, *337*(6092), 303-305.
2) Thakor, A. S., & Gambhir, S. S. (2013). Nanooncology: the future of cancer diagnosis and therapy. *CA: a cancer journal for clinicians*, *63*(6), 395-418.
3) Senapati, S., Thakur, R., Verma, S. P., Duggal, S., Mishra, D. P., Das, P., & Maiti, P. (2016). Layered double hydroxides as effective carrier for anticancer drugs and tailoring of release rate through interlayer anions. *Journal of Controlled Release*, *224*, 186-198.
4) Ladewig, K., Xu, Z. P., & Lu, G. Q. (2009). Layered double hydroxide nanoparticles in gene and drug delivery. *Expert Opinion on Drug Delivery*, *6*(9), 907-922.
5) Oh, J. M., Choi, S. J., Lee, G. E., Han, S. H., & Choy, J. H. (2009). Inorganic drug-delivery nanovehicle conjugated with cancer-cell-specific ligand. *Advanced Functional Materials*, *19*(10), 1617-1624.
6) Mok, H., Park, J. W., & Park, T. G. (2008). Enhanced intracellular delivery of quantum dot and adenovirus nanoparticles triggered by acidic pH via surface charge reversal. *Bioconjugate chemistry*, *19*(4), 797-801.
7) Singh, A. P., Biswas, A., Shukla, A., & Maiti, P. (2019). Targeted therapy in chronic diseases using nanomaterial-based drug delivery vehicles. *Signal transduction and targeted therapy*, *4*(1), 33.
8) He, C., Kim, S. W., & Lee, D. S. (2008). In situ gelling stimuli-sensitive block copolymer hydrogels for drug delivery. *Journal of controlled release*, *127*(3), 189-207.
9) Shi, J., Kantoff, P. W., Wooster, R., & Farokhzad, O. C. (2017). Cancer nanomedicine: progress, challenges and opportunities. *Nature reviews cancer*, *17*(1), 20-37.
10) Chan, W. C., Khademhosseini, A., Parak, W., & Weiss, P. S. (2017). Cancer: Nanoscience and nanotechnology approaches. *ACS nano*, *11*(5), 4375-4376.

11) Rosenblum, D., Joshi, N., Tao, W., Karp, J. M., & Peer, D. (2018). Progress and challenges towards targeted delivery of cancer therapeutics. *Nature communications*, *9*(1), 1410.

12) Darr, J. A., Zhang, J., Makwana, N. M., & Weng, X. (2017). Continuous hydrothermal synthesis of inorganic nanoparticles: applications and future directions. *Chemical reviews*, *117*(17), 11125-11238.

13) Ni, D., Bu, W., Ehlerding, E. B., Cai, W., & Shi, J. (2017). Engineering of inorganic nanoparticles as magnetic resonance imaging contrast agents. *Chemical Society Reviews*, *46*(23), 7438-7468.

14) Kwon, H. J., Shin, K., Soh, M., Chang, H., Kim, J., Lee, J., ... & Hyeon, T. (2018). Large-scale synthesis and medical applications of uniform-sized metal oxide nanoparticles. *Advanced Materials*, *30*(42), 1704290.

15) Qian, X., Liu, J., Fu, L., & Li, J. (2014). Quantum spin Hall effect in two-dimensional transition metal dichalcogenides. *Science*, *346*(6215), 1344-1347.

16) Liu, Z., Ma, L., Shi, G., Zhou, W., Gong, Y., Lei, S., ... & Ajayan, P. M. (2013). In-plane heterostructures of graphene and hexagonal boron nitride with controlled domain sizes. *Nature nanotechnology*, *8*(2), 119-124.

17) Wang, S., Li, X., Chen, Y., Cai, X., Yao, H., Gao, W., ... & Chen, H. (2015). A facile one-pot synthesis of a two-dimensional MoS2/Bi2S3 composite theranostic nanosystem for multi-modality tumor imaging and therapy. *Advanced Materials (Deerfield Beach, Fla.)*, *27*(17), 2775-2782.

18) Yoon, H. J., Kim, T. H., Zhang, Z., Azizi, E., Pham, T. M., Paoletti, C., ... & Nagrath, S. (2013). Sensitive capture of circulating tumour cells by functionalized graphene oxide nanosheets. *Nature nanotechnology*, *8*(10), 735-741.

19) Kalantar-Zadeh, K., & Ou, J. Z. (2015). T. daeneke, MS Strano, M. pumera and S. l. gras. *Adv. Funct. Mater*, *25*, 5086-5099.

20) Tran, T. T., Bray, K., Ford, M. J., Toth, M., & Aharonovich, I. (2016). Quantum emission from hexagonal boron nitride monolayers. *Nature nanotechnology*, *11*(1), 37-41.

21) Xue, C. C., Li, M. H., Zhao, Y., Zhou, J., Hu, Y., Cai, K. Y., ... & Luo, Z. (2020). Tumor microenvironment-activatable Fe-doxorubicin preloaded amorphous $CaCO_3$ nanoformulation triggers ferroptosis in target tumor cells. *Science advances*, *6*(18), eaax1346.

22) Xia, F., Wang, H., & Jia, Y. (2014). Rediscovering black phosphorus as an anisotropic layered material for optoelectronics and electronics. *Nature communications*, *5*(1), 4458.

23) Falin, A., Cai, Q., Santos, E. J., Scullion, D., Qian, D., Zhang, R., ... & Li, L. H. (2017). Mechanical properties of atomically thin boron nitride and the role of interlayer interactions. *Nature communications*, *8*(1), 15815.

24) Han, Q., Wang, X., Jia, X., Cai, S., Liang, W., Qin, Y., ... & Wang, C. (2017). CpG loaded MoS 2 nanosheets as multifunctional agents for photothermal enhanced cancer immunotherapy. *Nanoscale*, *9*(18), 5927-5934.

25) Oh, J. M., Park, M., Kim, S. T., Jung, J. Y., Kang, Y. G., & Choy, J. H. (2006). Efficient delivery of anticancer drug MTX through MTX-LDH nanohybrid system. *Journal of Physics and Chemistry of Solids*, *67*(5-6), 1024-1027.

26) Choy, J. H., Jung, J. S., Oh, J. M., Park, M., Jeong, J., Kang, Y. K., & Han, O. J. (2004). Layered double hydroxide as an efficient drug reservoir for folate derivatives. *Biomaterials*, *25*(15), 3059-3064.

27) Choy, J. H., Kwak, S. Y., Jeong, Y. J., & Park, J. S. (2000). Inorganic layered double hydroxides as nonviral vectors. *Angewandte Chemie International Edition*, *39*(22), 4041-4045.

28) Choy, J. H., Kwak, S. Y., Park, J. S., & Jeong, Y. J. (2001). Cellular uptake behavior of [γ-32P] labeled ATP–LDH nanohybridsElectronic supplementary information (ESI) available: histogram for Mg solubility of Mg2Al–LDH as a function of pH; FITC–LDH exchange rate according to NaCl concentration (FITC= fluorescein 5-isothiocyanate); cytotoxicity test of Mg2Al–NO3−–LDH. See http://www. rsc. org/suppdata/jm/b0/b008680k. *Journal of Materials Chemistry*, *11*(6), 1671-1674.

29) Choy, J. H., Kwak, S. Y., Park, J. S., Jeong, Y. J., & Portier, J. (1999). Intercalative nanohybrids of nucleoside monophosphates and DNA in layered metal hydroxide. *Journal of the American Chemical Society*, *121*(6), 1399-1400.

30) Choy, J. H., Oh, J. M., Park, M., Sohn, K. M., & Kim, J. W. (2004). Inorganic–biomolecular hybrid nanomaterials as a genetic molecular code system. *Advanced Materials*, *16*(14), 1181-1184.

31) Oh, J. M., Choi, S. J., Kim, S. T., & Choy, J. H. (2006). Cellular uptake mechanism of an inorganic nanovehicle and its drug conjugates: enhanced efficacy due to clathrin-mediated endocytosis. *Bioconjugate chemistry*, *17*(6), 1411-1417.

32) Oh, J. M., Hwang, S. H., & Choy, J. H. (2002). The effect of synthetic conditions on tailoring the size of hydrotalcite particles. *Solid State Ionics*, *151*(1-4), 285-291.

33) Vaccari, A. (1998). Preparation and catalytic properties of cationic and anionic clays. *Catalysis today*, *41*(1-3), 53-71.

34) Zhang, Y., Cheng, X., Wu, C., Köhler, J., & Deng, S. (2019). Electronic structure and lithium diffusion in LiAl2 (OH).6Cl^- studied by first principle calculations. *Molecules*, *24*(14), 2667.

35) Dutta, P.K.; Puri, M. Anion-exchange in lithium aluminate hydroxides. J. Phys. Chem. 1989, 93, 376–381.

36) Fogg, A.M.; O'Hare, D. Study of the intercalation of lithium salt in gibbsite using time-resolved in situ X-ray diffraction. Chem. Mater. 1999, 11, 1771–1775.

37) Lei, L.X.; Vijayan, R.P.; O'Hare, D. Preferential anion exchange intercalation of pyridinecarboxylate and toluate isomers in the layered double hydroxide [LiAl2 (OH)6]Cl H2O. J. Mater. Chem. 2001, 11, 3276–3280.

38) Hou, X.Q.; Bish, D.L.; Wang, S.L.; Johnston, C.T.; Kirkpatrick, R.J. Hydration, expansion, structure, and dynamics of layered double hydroxides. Am. Mineral 2003, 88, 167–179.

39) Fogg, A.M.; Rohl, A.L.; Parkinson, G.M.; O'Hare, D. Predicting guest orientations in layered double hydroxide intercalates. Chem. Mater. 1999, 11, 1194–1200.

40) Hou, X.J.; Li, H.Q.; He, P.; Sun, Z.H.; Li, S.P. Structural and electronic analysis of Li/Al layered double hydroxides and their adsorption for CO_2. Appl. Surf. Sci. 2017, 416, 411–423.

41) Hou, X.Q.; Kalinichev, A.G.; Kirkpatrick, R.J. Interlayer structure and dynamics of Cl- -LiAl2 -layered double hydroxide: Cl-35 NMR observations and molecular dynamics modeling. Chem. Mater. 2002, 14, 2078–2085.

42) Hou, X.Q.; Kirkpatrick, R.J. Thermal evolution of the Cl^- -LiAl2 layered double hydroxide: A multinuclear MAS NMR and XRD perspective. Inorg. Chem. 2001, 40, 6397–6404.

43) Hakeem, A., Zhan, G., Xu, Q., Yong, T., Yang, X., & Gan, L. (2018). Facile synthesis of pH-responsive doxorubicin-loaded layered double hydroxide for efficient cancer therapy. *Journal of Materials Chemistry B*, *6*(36), 5768-5774.

44) Thorn, C. F., Oshiro, C., Marsh, S., Hernandez-Boussard, T., McLeod, H., Klein, T. E., & Altman, R. B. (2011). Doxorubicin pathways: pharmacodynamics and adverse effects. *Pharmacogenetics and genomics*, *21*(7), 440.

45) Aluker, N. L., Herrmann, M. E., & Suzdaltseva, Y. M. (2019). A spectrophotometric study of nitrate and nitrite salts and their aqueous solutions. *Optics and Spectroscopy*, *127*, 991-996.

46) Bansal, R., Singh, R., & Kaur, K. (2021). Quantitative analysis of doxorubicin hydrochloride and arterolane maleate by mid IR spectroscopy using transmission and reflectance modes. *BMC chemistry*, *15*(1), 1-11.

47) Nakatuka, Y., Yoshida, H., Fukui, K., & Matuzawa, M. (2015). The effect of particle size distribution on effective zeta-potential by use of the sedimentation method. *Advanced Powder Technology*, *26*(2), 650-656.

48) dos Santos Macedo, R., Fazzi, R. B., da Costa Ferreira, A. M., & Constantino, V. R. L. (2020). Cobalt-based layered double hydroxides revisited: evidence for oxidizing radical generation. *New Journal of Chemistry*, *44*(24), 10022-10032.

49) Paarakh, M. P., Jose, P. A., Setty, C. M., & Peterchristoper, G. V. (2018). Release kinetics–concepts and applications. *International Journal of Pharmacy Research & Technology (IJPRT)*, *8*(1), 12-20.

50) Anubhav Jain, Shyue Ping Ong, Geoffroy Hautier, Wei Chen, William Davidson Richards, Stephen Dacek, Shreyas Cholia, Dan Gunter, David Skinner, Gerbrand Ceder, Kristin A.

Persson; Commentary: The Materials Project: A materials genome approach to accelerating materials innovation. APL Mater 1 July 2013; 1 (1): 011002.

51) de Almeida, M. S., Susnik, E., Drasler, B., Taladriz-Blanco, P., Petri-Fink, A., & Rothen-Rutishauser, B. (2021). Understanding nanoparticle endocytosis to improve targeting strategies in nanomedicine. *Chemical Society Reviews*, *50*(9), 5397-5434.

52) Merghoub, N., Benbacer, L., Terryn, C., Attaleb, M., Madoulet, C., Benjouad, A., ... & Amzazi, S. (2011). In vitro antiproliferative effect and induction of apoptosis by Retama monosperma L. extract in human cervical cancer cells. *Cellular and Molecular Biology*, *57*(2), 1581-91.

53) Gajadeera, C., Willby, M. J., Green, K. D., Shaul, P., Fridman, M., Garneau-Tsodikova, S., ... & Tsodikov, O. V. (2015). Antimycobacterial activity of DNA intercalator inhibitors of Mycobacterium tuberculosis primase DnaG. *The Journal of antibiotics*, *68*(3), 153-157.

54) Kumral, A., Soluk-Tekkeşin, M., Olgaç, V., Doğru-Abbasoğlu, S., Türkoğlu, Ü., & Uysal, M. (2016). Beneficial effects of carnosine and carnosine plus vitamin E treatments on doxorubicin-induced oxidative stress and cardiac, hepatic, and renal toxicity in rats. *Human & experimental toxicology*, *35*(6), 635-643.